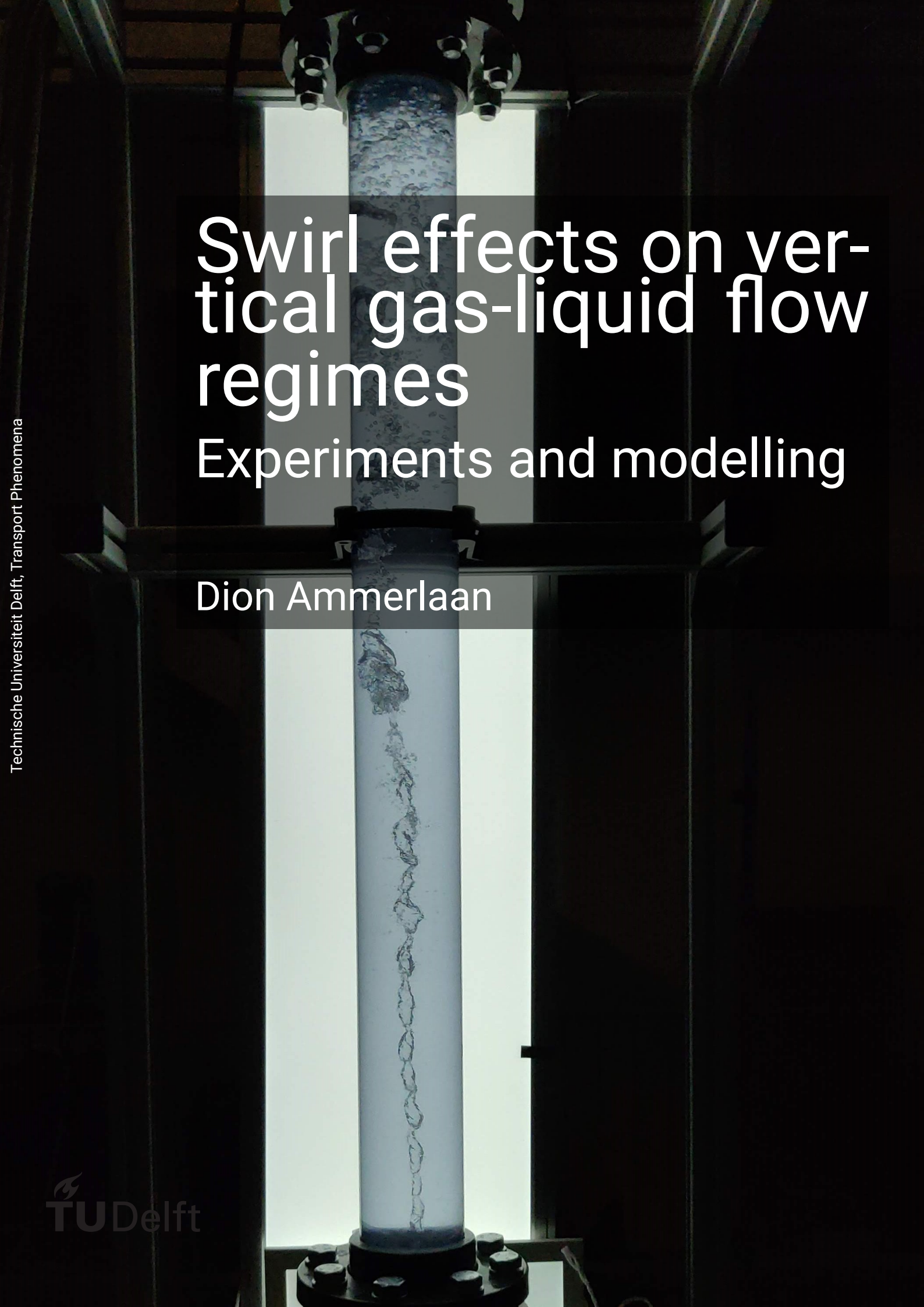

Swirl effects on vertical gas-liquid flow regimes

Experiments and modelling

Dion Ammerlaan

Technische Universiteit Delft, Transport Phenomena

TU Delft

Swirl effects on vertical gas-liquid flow regimes

Experiments and modelling

by

Dion Ammerlaan

to obtain the degree of Master of Science
at the Delft University of Technology,
to be defended publicly on Tuesday May, 2020 at 10:00 AM.

Student number:	4629213	
Project duration:	September 12, 2020 – May, 2021	
Thesis committee:	Dr. L. Portela,	TU Delft, supervisor
	Prof. Dr. ir. R.A.W.M. Henkes,	TU Delft 2nd examinor
	Dr. ir. G.M.H. Meesters,	3th examinor

TU Delft

Abstract

Even though the world's energy production is shifting towards renewable energies, oil is still needed during the transition towards a society with a fully renewable energy generation. Inline swirl separators and hydroclones are widely used in the oil industry to separate oil from water. In order to investigate the possibilities and limitations of real-time control of an inline swirl separator, a simplified facility operating with air and water was built at TU Delft as part of the TOMOCON project. It is important to know the behaviour of the flow inside the separator when choosing the operational conditions and designing the controllers. Therefore, an identification of the different flow regimes created inside the device at different swirl intensities is explored in this thesis. The first objective of this thesis, was to investigate the effect of different swirl strengths on the flow regime maps. In this thesis, flow regime maps are generated for flows brought in rotation via an axial swirl generator. For these maps, four different swirl elements with similar geometries but with different vane angles were used to investigate the effect of the strength of the swirl element on flow regime maps. The influence of swirl decay on the flow regime maps was also investigated, by observing the flow further downstream inside the separator. A second objective of this thesis was to propose the start of a mechanistic model which tries to guess where the transition from regular flow patterns to flow patterns with a gas core. The experiments were in a range of $0.03\,\mathrm{m\,s^{-1}}$ to $0.70\,\mathrm{m\,s^{-1}}$ for the liquid superficial velocity (u_{sl}) and between $0.02\,\mathrm{m\,s^{-1}}$ to $1.00\,\mathrm{m\,s^{-1}}$ for the gas superficial velocity (U_{sg}).

The results showed that the formation of the gas core close to the swirl element is fully dependent of the liquid flow rate and independent of the gas flow rate. It was also shown that this liquid superficial velocity where the transition happens depends strongly on the strength of the swirl element used: the superficial velocity increases as the swirl element gets weaker. An important result that followed from this is: the gas column close to the swirl element forms for a constant product of u_{sl} and $Tan(\Theta)$, where Θ is the vane angle of the swirl element, such that $u_{sl} \cdot \tan(\Theta) = 0.25$

The flow regime maps made further away from the swirl element to investigate the effect of decay, showed an important difference with those made close to the swirl element: the maps further away from the swirl element showed a dependency on the gas flow rate. Moreover, the liquid superficial velocity is shifted to higher values due to the decay of the swirl along the pipeline.

The second main objective was to construct the beginning of a mechanistic model, to predict the transition from flow types without a gas column to flow types with a gas column. A model was constructed based on the pressure difference between the wall and gas-liquid interface. For this model, it is assumed that flow separation already happens inside the swirl element, such that the tangential velocity (u_θ) in the pipe could be determined. The results showed that for a low flow rate of gas, the model predicts the transition from non-columnar to columnar flow patterns relatively well. The pressure difference between the wall and the gas core was roughly constant for each swirl element, meaning that the driving force for the separation was similar. When the gas flow rate was increased, the pressure difference was lower, while also spanning a larger, such that it could not be considered constant anymore. This indicates that either unforeseen effects came into play or that the driving force for the column is not always the same. Further away from the swirl element, the pressure difference was slightly lower for a situation with a low gas flow rate, when comparing it to the pressure difference close to the swirl element. It also has a slightly larger range further away from the swirl element. For higher gas flow rates, there was a large range of pressure differences between swirl elements, indicating that the driving force might not always be the same. The model was checked with data found in literature and did not match, as the pressure differences were higher for a smaller diameter. There appears to be a ratio between the cross-sectional area and pressure difference and this should be investigated in further research.

Acknowledgements

First and foremost, I want to express my gratitude towards Professor Luis Portela for giving me the opportunity to do my master thesis and guiding me during the whole project. His knowledge on fluid dynamics has been immensely useful during the meetings we have had. Furthermore, I want to express my gratitude towards Matheus Martinez Garcia who was my daily supervisor during this project. His help ranged from explaining topics which I was struggling with too together thinking about the model proposed in this thesis and all of his help was highly appreciated. I also want to thank all of the bachelor, master and Phd students of the TP group for either having discussions about my thesis or the nice conversations we have had during the breaks.

Contents

List of Figures

List of Tables

Nomenclature

Roman symbols

$\dot{m}_i$	Mass flux	$\mathrm{kg\,s^{-1}}$
A_i	Area	$\mathrm{m^2}$
C_{decay}	Decay factor	-
D	Pipe diameter	m
f_i	Interfacial friction factor	-
$F_{buoyancy}$	Buoyancy force	N
$F_{inwards}$	Centripetal force	N
$F_{outwards}$	Centrifugal force	N
g	Gravitational Constant	$9.81\,\mathrm{m\,s^{-2}}$
l_e	Entrance length	m
L_i	Angular momentum flux	$\mathrm{kg\,m^2\,s^{-2}}$
N_{frames}	Number of frames within a time span	-
p	Pressure	$\mathrm{N\,m^{-2}}$
Q	Volumetric flow	$\mathrm{m^3\,s^{-1}}$
R	Pipe radius	m
R_c	Critical core radius	m
R_g	Gas core radius	m
u_b	Bulk velocity	$\mathrm{m\,s^{-1}}$
$u_{\theta,i}$	Azimuthal/tangential velocity	$\mathrm{m\,s^{-1}}$
$u_{r,i}$	Radial velocity	$\mathrm{m\,s^{-1}}$
$u_{s,i}$	Superficial velocity	$\mathrm{m\,s^{-1}}$
$u_{z,i}$	Axial velocity	$\mathrm{m\,s^{-1}}$
V_b	Bubble Volume	$\mathrm{m^3}$
z	Axial position	m
z_r	Reference axial position	m

Greek symbols

α_i	Void fraction	-
Δp	Pressure difference between the interface and the wall	Pa
ΔR^2	$R^2 - R_g^2$	$\mathrm{m^2}$

ΔR^3	$R^3 - R_g^3$	m^3
ν	Kinematic viscosity	$\mathrm{m}^2\,\mathrm{s}^{-1}$
Ω	Swirl number	-
ϕ_i	Volumetric flow rate	$\mathrm{L\,min}^{-1}$
ρ_i	Density	$\mathrm{kg\,m}^{-3}$
σ	Surface tension	$\mathrm{N\,m}^{-1}$
Θ	Vane angle	$^\circ$

Subscripts

0	Values at the exit of the swirl element
b	Bulk phase in the axial direction
c	Continuous phase
$core$	Values in the core
d	Dispersed phase
g	Gas phase
l	Liquid phase
$pipe$	Pipe
se	Swirl element

1 Introduction

Although more and more energy is generated by renewable energy and societies are transitioning towards a fully renewable energy generation, the demand for fossil fuels is still high. In order to satisfy this need for fossil fuels, new oil wells have to be opened continuously. These wells are in ever increasing depth, so called deep water basins. In these deep water basins the oil is captured under an impermeable material, a layer of water is also present however this remains under the oil due to the density difference between the two components [1, 2].

As these deep water basins mature, more and more water is extracted from the wells together with the oil, the water flows with the oil due to the viscosity difference making the water flowing more easily than the oil. In the North Sea the water cut increases in a different way, here the pressure in the fields is maintained by pumping water or gas in the fields[3]. This causes the water cut to be even higher than in a deep water platforms as those which are found for example in the Gulf of Mexico. It is more costly to pump this mixture to the shore as the hydrostatic pressure losses are greater for a larger flow. To safe on pumping costs, the water and oil are separated on the oil platform.

The current way to separate the water and oil on the oil platforms is with the use of gravity tanks which is are density-driven separators. For the water and oil to be fully separated, the residence time of the mixture has to be longer than the settling time. As the difference in density between water and oil is not that large, the settling time is long. This long separation time translates into large gravity tanks with lengths that can range up to 25 meter with and diameters of 3 meter to fully separate the flow of water and oil[4, 5].

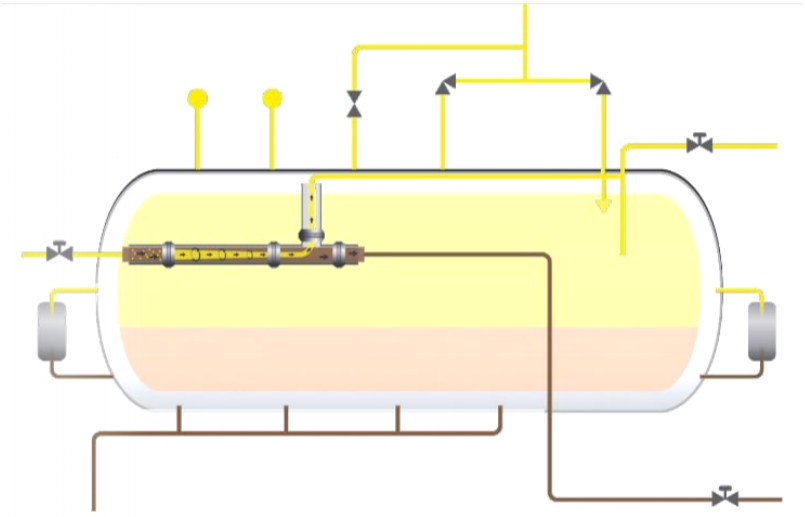

Figure 1.1: Difference in size between a gravity separator tank and an inline fluid separator[5]

As big gravity tanks are unwanted due to their size which is connected to the costs to install them on a platform, hydrocyclones, often referred to as cyclones, are employed to speed up separation while taking up less space. Cyclones generate centrifugal forces through rotating fluids which can be much larger than the gravitational force thus accelerating separation of the different fluids.

Two types of hydrocyclones are generally used, tangential and axial which are differentiated by their mode of input and output. Tangential cyclones have been around since the late 1800s but extensive use did not start until the 1950s while their use in oil-water separation did not start until the 1980s [6]. In a tangential cyclone mixture is fed tangentially in order to generate a rotating motion. The denser phase or fluid leaves at the bottom of the cyclone while the less dense leaves at the top. An Axial cyclone for fluid-fluid separations was first proposed by Dirkzwager [6] as a new way to separate oil from water. In an axial cyclone the rotating motion of the fluids is generated by a static swirl element in the axial direction. The lighter phase travels inwards and is collected by a pickup tube. The differences can be seen in figure 1.2.

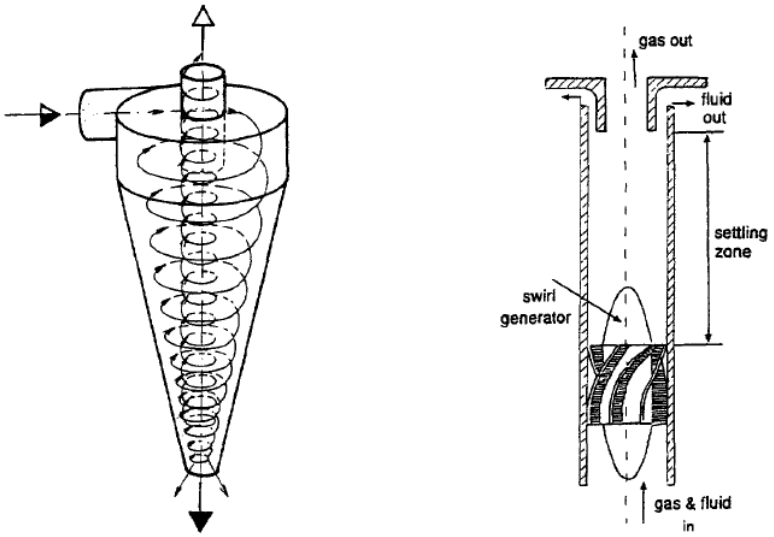

Figure 1.2: Illustration of tangential (left) and axial (right) cyclones where the difference in injection strategy can be clearly seen, illustration was taken from Dirkzwager[6]

Axial cyclones have some advantages over tangential cyclones which include lower pressure drop, less turbulence and a more compact design[6, 7]. Since the first proposition of the axial cyclone separator by Dirkzwager, research has been done on optimisation of the swirl angle, mapping of the swirl patterns and determining separation efficiencies for varying conditions[7–9]. On top of the fact that an inline fluid separator, which uses an axial cyclone, takes up less space and they are also inherently safer. This is due to the fact that an inline fluid separator has a much smaller volume and thus contains less hydrocarbons.

As presented in Figure 1.2, an inline swirl separator is composed of pipe that contains a mixture of two phases, a static swirl element which induces the swirl and a pick-up tube which collects the less dense fluid. The swirl generates an centrifugal force of up to hundreds of times the gravitational acceleration (g), this causes the less dense fluid to migrate into the centre of the tube so it can flow out into the pick-up tube. At the Delft University of Technology, such a setup has been built which this thesis will make use of. This setup was constructed for the TOMOCON project. The aim of this project is to provide a proof of concept of tomography for real time control of industrial processes, among these processes is the separation of two phases using an inline swirl separator. As the focus is on understanding the physics of the separation and applying it on a proof of concept control of the inline swirl separator, a mixtureof air and water is used in the experiments. This also helps with the visualisation of the flow and separation, this further helps to understand the physics behind the separation processes. This thesis will make use of the TOMOCON setup and therefore also use the mixture of water and air.

1.1. Research of this thesis

As a water air mixture is now used in the inline swirl separator, it will be useful to know the flow regimes present in the swirling gas liquid flows. As the different regimes may be dominated by different physics, they can effect the operational regimes that can be considered by the controller. For the control of separation first a gas core has to form in the middle of the pipe.

A lot of attention has been given to multiphase flows in pipelines, this includes but is not limited to identifying the flow patterns present in pipe flow and constructing flow regime maps based on these patterns[10]. For industrial processes, it is useful to know the nature and dynamics of gas-liquid flow systems. The research on this started in the 1960's and 1970's with the identification of the flow regimes present in gas-liquid multiphase flows[10], this identification was done visually or with a measuring technique such as X-ray pictures[11, 12]. These flow types showed very different dynamic behaviour between them, so knowing when each flow regime is needed when designing a process which uses gas liquid flows. Based on the identified patterns, flow regime maps can be constructed, which show where each identified pattern is present [12, 13].

These flow regime maps can be constructed based on experimental data, the gas and liquid are varied in a range and the flow patterns are recorded [11, 13]. The approach is however limited to the geometry and phase properties used. Another way of constructing these flow regime maps is based on mechanistic models. These mechanistic models predict when each flow regime is present based on phase properties and system geometry. With these mechanistic models, the appearance of the flow regimes can be predicted without having to do experiments, which is a big advantage.

Although a lot of work has been performed in understanding multiphase flows in both vertical and horizontal pipelines and consequently constructing flow regime maps for these systems, the same attention has not been given to construct similar flow regime maps for swirling multiphase flows. Some research has been performed to map a single swirl element and identify the patterns present in these swirling multiphase flows, the influence of different swirl elements has not been researched thoroughly [8, 14–16]. Furthermore, while there are many models for the transition criteria in regular multiphase flows, these are not yet constructed for the swirling multiphase flow regimes. These swirling multiphase flow patterns also have some others use apart from those linked to oil separation, in nuclear reactors, axial cyclones can be used in boilers to improve heat transfer in flow boiling heat transfer [8, 17].

As briefly mentioned, there has been limited research in the effect of the swirl element on the flow regime maps of swirling flows. This thesis will therefore be a spiritual continuation of the work started in the 1960's. The focus will be on visually identifying the flow patterns in swirling gas-liquid vertical flows. As there is almost no research done on the effect of using different swirl strengths on the flow regime maps, this will also be an important topic of this thesis. Furthermore, it will be investigated if a mechanistic model for the transitions in the swirling gas-liquid flow regimes can be constructed. This thesis will therefore try to answer two different research questions:What is the influence of using different strengths of swirl elements on the flow regime maps? and is it possible to construct a mechanistic model to predict the flow patterns present in swirling flow? The TOMOCON setup, which is an inline swirl separator, will be used to identify the patterns and for this setup the flow.

1.2. Thesis outline

To answer these two research questions, the thesis is divided into six chapters. The first chapter, which is the current chapter, goes into the background of the research performed in this thesis and explains the need for axial cyclones. The second chapter will focus around the governing equations for swirling flow and the relevant theory. In the third chapter a proposition is done fore a mechanistic model which predicts the transition between flow types with and without a gas column. In the fourth chapter the setup used is discussed in detail as well as a description for the various experiments performed. The results and discussion are shown in chapter 5, after which the conclusion and some recommendations are done in chapter 6.

2

Theory

2.1. Multiphase flows

To understand the flow patterns of a swirling flow, the patterns of regular gas-liquid multiphase flow first have to be understood. As briefly mentioned in the introduction 1, extensive research has been performed in the field of gas-liquid flows and pipelines. For vertical upward gas-liquid flow in a pipe there are four main flow types present namely: Bubbly flow, Slug or Plug flow, Churn flow and Annular flow [12, 18]. A sketch of these can be seen in figure 2.1

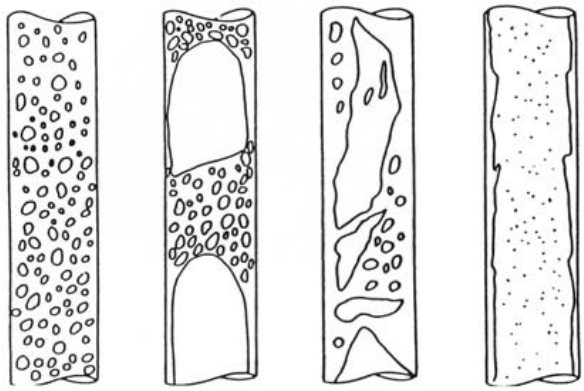

Figure 2.1: An overview of the main flow patterns of gas-liquid vertical flow, from left to right with an increase in gas flow: Bubbly flow, Slug flow, Churn flow, Annular Flow. The flow direction is upwards. [18]

Bubbly flow is characterised by discrete bubbles which are dispersed throughout a continuous liquid phase. Bubbly flow can be present two forms, regular bubbly flow and dispersed bubbly flow. Regular bubbly flow is only present at low liquid and gas superficial velocities. In this region bubbles can already coalesce and form slightly larger bubbles, as the liquid does not yet have enough turbulence to continuously break up the bubbles. When the liquid flow rate is high enough, the turbulence continuously breaks up the bubbles in the flow causing only small bubbles to appear. The transition between bubbly and dispersed bubbly flow can be described by the following equation derived by Taitel et al.[19], which is based on a balance of turbulent fluctuations of the flow, that tends to break up the bubbles and the surface tension of the bubbles, that attempts to balance the effect keeping the flow bubbly.

$$u_{ls} = -u_{gs} + 4.0\left(\frac{D^{0.429}(\sigma/\rho_l)^{0.089}}{\nu_l}\left(\frac{g(\rho_l-\rho_g)}{\rho_l}\right)^{0.446}\right) \tag{2.1}$$

In this equation u_{sl} is the superficial liquid velocity, u_{sg} is the superficial gas velocity , D is the pipe diameter , σ is the surface tension between the respective phases, ρ_l is the liquid density, ν_l is the liquid kinematic viscosity, g is the gravitational constant and ρ_g is the density of the gas.

If the starting situation is regular bubbly flow at a lower liquid flow and the gas flow rate is increased, bubbles will start to coalesce and larger bubbles form. When these bubbles almost reach the size of the pipe diameter, the flow type has transformed into slug flow, which is also referred to as plug flow [11, 19]. The large bubbles, also called Taylor bubbles, usually have a bullet shape or spherical cap, a sketch of this can be seen

in the second illustration of figure 2.1. A liquid film is present between the pipe wall and the Taylor bubble, where the liquid flow direction can be downwards even though the net flow is still upwards. The transition between bubbly and slug flow is based on the void fraction of the flow and the relative rise velocity of the gas. The transition from bubbly to slug flow happens at a void fraction of 0.25, as the coalescence severely increase for a void fraction larger than 0.25. The homogeneous void fraction is calculated as

$$\alpha_g = \frac{u_{sg}}{u_{sg} + u_{sl}} \tag{2.2}$$

Where α_g is the void fraction of gas. For a similar flow rate, the velocities of gas and liquid are not the same due to the rise velocity of the gas inside the liquid, in form of an equation this is expressed as

$$u_l = u_g - u_0 \tag{2.3}$$

Here u_l is the liquid velocity, u_g is the gas velocity and u_0 is the rise velocity of the gas. Harmathy has shown that the rise velocity of relatively large bubbles, still being in the bubbly pattern, is not that sensitive to the bubble size [20] The rise velocity is given by

$$u_0 = 1.53\left(\frac{g(\rho_l - \rho_g)\sigma}{\rho_l^2}\right)^{0.25} \tag{2.4}$$

The parameters u_g and u_l in equation 2.3 can be replaced by their respective superficial velocities according to

$$u_l = \frac{u_{sl}}{1 - \alpha_g} \tag{2.5}$$

$$u_g = \frac{u_{sg}}{\alpha_g} \tag{2.6}$$

Such that the total equation predicting the transition between the bubbly and slug flow patterns becomes equation 2.8

$$u_{sl} = \frac{1 - \alpha_g}{\alpha_g} u_{sg} - 1.53(1 - \alpha_g)\left[\frac{g(\rho_l - \rho_g)\sigma}{\rho_l^2}\right]^{1/4} \tag{2.7}$$

$$u_{sl} = 3.0 u_{sg} - 1.15\left[\frac{g(\rho_l - \rho_g)\sigma}{\rho_l^2}\right]^{1/4} \tag{2.8}$$

In the region where the dispersed bubbly is present, slug flow cannot exist as the bubbles are continuously broken up, for this reason bubbly flow can exist for larger void fractions than 0.25 of which the limit is the maximum packing void fraction of 0.52. Furthermore, the rise velocity of bubbles can be neglected in this region so the transition becomes

$$u_{sl} = \frac{1 - \alpha_g}{\alpha_g} u_{sl} \tag{2.9}$$

$$u_{sl} = 0.92 u_{sl} \tag{2.10}$$

Increasing the gas rate even further from slug flow on will result in churn flow. This flow type is characterised as a chaotic flow which is somewhat similar to slug flow. The Taylor Bubbles which are present in the slug flow are distorted in churn flow and do not bridge the full width of the pipe anymore. The liquid slugs which separated the Taylor bubbles can be destroyed when the gas fraction within becomes to high, causing the liquid to fall. The liquid is then collected at a lower level and forms a bridge again restoring the slug, this process is observed as a sort of oscillatory motion [11, 19]. The transition between slug and churn flow can be seen as entrance behaviour and therefore depends on the entrance length and the pipe diameter and is modelled as follows [19]

$$u_{sl} = -u_{sg} + \sqrt{gD}\left(\frac{l_E}{40.6D} - 0.22\right) \tag{2.11}$$

In this equation l_E is the entrance length, this is the point at which the flow patterns are recorded.

At even higher gas flow rates, the churn flow starts transforming into annular flow. Annular flow is characterised by a thin wavy film of liquid at the wall with a continuous gas core containing small droplets in the middle of the pipe. The transition from churn to annular is modelled according to equation 2.12:

$$u_{sg} = \frac{3.1\sigma g(\rho_l - \rho_g)^{1/4}}{\rho_g^{1/2}} \tag{2.12}$$

For an system with water and air, this transition happens at a superficial air velocity of around 11 m/s.

With all the equations known for the respective transitions between patterns, a flow pattern map can be constructed. Using the values given in chapter 4 for the system used in this thesis the theoretical flow pattern map upstream of the swirl element is shown in Figure 2.2

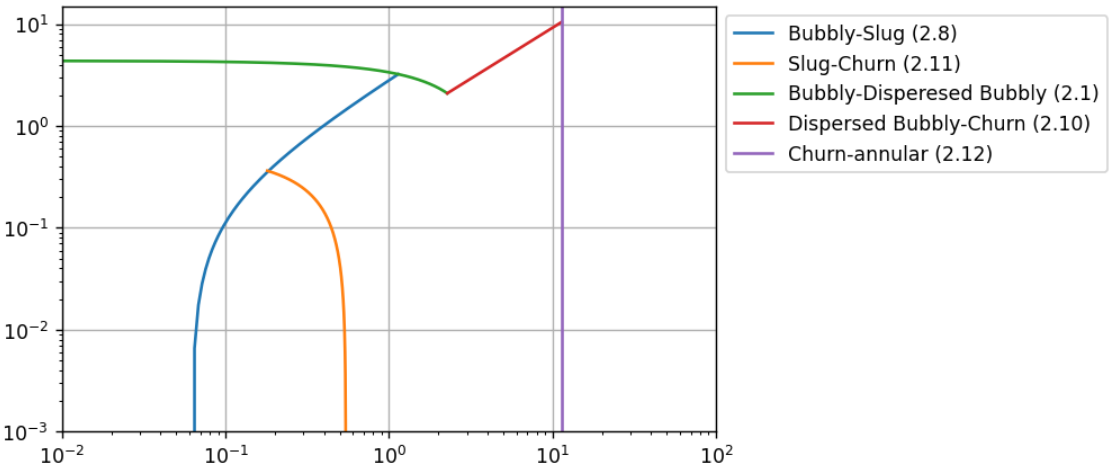

Figure 2.2: Theoretical flow regime map of the system used in this thesis

2.2. Swirling multiphase flows

2.2.1. Forces acting on the fluids

In an inline flow separator the separation of phases is achieved by rotating the flow. When the fluid is brought in a rotating motion, additional forces will start playing a role in the formation of patterns. When a tangential velocity is introduced, a radial pressure gradient will be balancing the centrifugal force generated by the liquid. It is well known that the pressure difference in the r-coordinate scales with tangential velocity and radius, such that the pressure difference in r becomes [21]

$$\frac{\partial p}{\partial r} = \rho_l \frac{u_\theta^2}{r} \tag{2.13}$$

$$\Delta p \sim \rho_l u_\theta^2 \tag{2.14}$$

When a bubble is injected in the domain, this pressure distribution inside the liquid phase generates a resultant force pointing inwards, which is described by

$$F_{inwards} = \frac{V_b \rho_c U_\theta^2}{r} \tag{2.15}$$

Here ρ_c is the density of the continuous phase and U_θ is the tangential velocity at the radius r, V_d is the volume of a bubble. The opposite of the centripetal force is the centrifugal force of the bubble which is pointed away from the centre of the pipe

$$F_{outwards} = \frac{V_b \rho_d U_\theta^2}{r} \tag{2.16}$$

ρ_d is the density of the pocket of air. The balance of the centripetal and centrifugal force act as a buoyancy force, this acts similar to the balance of forces generated by gravity, but is now pointed towards the pipe centre. The buoyancy forces causes a less dense fluid to move inwards in a rotating medium while the denser fluid moves outwards. The equation for the buoyancy force is given by

$$F_{buoyancy} = \frac{V_b \Delta\rho U_\theta^2}{r} \tag{2.17}$$

Where $\Delta\rho$ is the density difference between the respective mediums. This buoyancy force is responsible for creating the gas core and the swirl patterns, as it forces the air to accumulate in the centre of the pipe.

2.2.2. Vortex types

When the fluids are brought into a rotating motion, certain types of structure will appear in the tangential velocity profiles, the so called vortex types. For vortex types based on the tangential velocity their are two main types: the Rankine and Gaussian vortex[22]. The Rankine vortex is characterised by inner region which resembles a forced vortex in the centre region where u_θ increases with r and an outer region where u_θ decreases for increasing r. An Gaussian has an inner core which somewhat resembles a forced vortex and has an outer region where the tangential velocity decreases for increasing r. The vortexes generated in this thesis somewhat resemble a Rankine vortex as can be seen from experimental data obtained by Van Campen [1], an example of this data can be seen in Figure 2.3. This data shows that the distribution is not exactly a Rankine vortex but rather a forced vortex in the inner region, with a roughly constant velocity in the outer region.

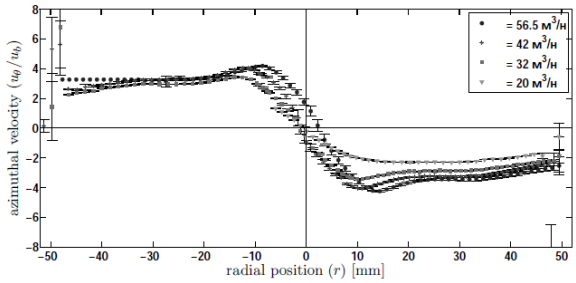

Figure 2.3: The tangential velocity distribution of a swirling flow in a pipeline, obtained from Van Campen [1]

The tangential velocity distribution within the vortex as seen in Figure 2.3 can be described by the following equation

$$u_{\theta,0} = \begin{cases} \frac{r}{R_c} u_{\theta,max} & \text{for } 0 \leq r < R_c \\ u_{\theta,max} & \text{for } R_c \leq r \leq R \end{cases} \tag{2.18}$$

Here $u_{\theta,0}$ is the tangential velocity right after the swirl element, R_c is the critical core radius and $u_{\theta,max}$ is the maximum tangential velocity. According to Van Campen[1] the transition from the inner to outer region happens at a $R_c = 0.25R$

2.2.3. The swirl number

An important characteristic of swirling flows is the Swirl number which is a non-dimensional number. The swirl number is an indication of the amount of swirling motion present in the system and is defined as the azimuthal momentum flux made dimensionless using the pipe radius, density and the bulk velocity. For a single phase flow, the swirl number is given as:

$$\Omega = \frac{\int_0^R 2\pi\rho u_z u_\theta r^2 \, dr}{\pi\rho R^3 u_b^2} \tag{2.19}$$

Here Ω represents the swirl number, ρ the density of the continuum phase, u_z is the axial velocity, u_θ is the azimuthal velocity, u_b is the bulk velocity and R is the radius of the pipeline. The swirl number for the geometry used in this thesis can be approximated with the following equation

$$\Omega = 2.043 \tan(\theta) \tag{2.20}$$

Where θ is the vane angle. A derivation for this equation can be found in appendix A

Due to friction with the wall, the tangential velocity decays over the length of the tube and with it the swirl number. The decay of the swirl number over the length of the pipe is described by Kitoh and Dirkzwager [6, 21] according to equation 2.21. This equation is only valid for very small swirl numbers, however experimental data showed that it is still a good approximation for the decay of the swirl number even for larger swirl numbers[21].

$$\Omega = \Omega_0 exp\left(-C_{decay}\frac{z-z_r}{D}\right) \tag{2.21}$$

Here Ω_0 is the swirl number at a reference location, C_{decay} is a decay factor which is obtained from experimental data and was found to be 0.04 [1, 23], z_r is the reference position and D is the diameter of the tube.

2.2.4. Swirling flow types

In relation to the classical gas-liquid vertical flow patterns, additional flow regimes appear in swirling flows. The four main flow types, bubbly, slug, churn and annular are still present though a swirling motion can be observed depending on the flow rates.

If the incoming flow to the swirl element is a form bubbly flow, a swirling column or swirling gas column can be formed when the liquid flow rate is sufficiently high [8]. In this flow pattern, all of the gas has migrated towards the centre of the pipeline to form a gas column, an example can be seen in figure 2.4a. This is a highly stable flow pattern though some slight pulsations can be seen which originate from slightly larger bubbles upstream of the swirl element. In this thesis, a swirling column is only present if the gas core reaches the first flange in the downstream section, approximately 20 cm downstream of the swirl element. This flow type can also be present near the pick up tube, here the definition for a swirling column is similar to that near the swirl outlet however it has to reach the pick up tube.

When a swirl column is present and the gas rate is increased, the flow type at the outlet of the swirl also changes. In literature this has been called a swirling intermittent flow [8, 14]. The swirling intermittent flow still has a gas column in the middle of the pipe however, due to the incoming slugs or larger bubbles, this gas column 'pulsates', this can also be observed in Figures 2.4b and 2.4c. In this thesis two sub patterns are introduced in the swirling intermittent region, these are the 'Swirling pulsating' and the 'Swirling burst' flow patterns. Both of these patterns contain the pulsating nature that differentiates them from the swirling column flow type. The differences between the swirling pulsating and swirling burst mainly originate in the size and stability of the gas core. The swirling pulsating pattern has smaller pulsations and the core remains intact which can be observed in Figure 2.4b. At the bottom of this figure, a bigger gas column can be seen coming into the picture while further downstream a smaller gas column is observed.

When the gas flow rate is further increased from the swirling pulsating pattern on, the second sub pattern starts appearing. The swirling burst pattern is similar to that of the swirling pulsating, however the swirling burst has larger pulsations, on top of this, the core can sometimes 'break' causing small bubbles to appear again which can be seen in Figure 2.4c. Sudden contractions of the core also appear which can be seen in too in figure 2.4c. For both of these flow patterns, the column that is formed has to reach the first flange similarly to the swirling column pattern.

In this thesis a new pattern will be introduced named: 'Swirl dying', which as the name suggests, is a swirl which has decayed until the point where it does not from a gas column anymore, as can be seen in figure 2.4d. This pattern is introduced as the patterns close to the pick up tube are also of interest in this thesis, as the dying swirl is not something that could be described by the classical patterns or the swirling patterns. The swirl dying is characterised by a more helical flow of the remains of the core where big pockets of air are still present. The definition that will be maintained in this thesis for a flow pattern to be referred to as swirl dying is that it has to have a stable column up until around 34 cm before the pick up tube. A detailed description on the visualisation of the flow patterns can be found in chapter 4

As the flow patterns are dynamic and not static, single images do not well represent the actual behaviour of the flow patterns. Therefore, sequences of images for each flow pattern are shown in Appendix B to properly show the behaviour of the patterns. For the rest of this thesis, the patterns will be referred to by their name, or if talked about as a group they are referred to as columnar flow types.

2.3. Estimation for the tangential velocity in the pipe

As one of the goals of this this is to predict when the transition from non-swirling patterns to swirling patterns takes place, some parameters will have to be calculated. An important parameter for this will be the tangential velocity (u_θ), that is responsible for pushing the air to the centre of the pipe. The tangential velocity profile

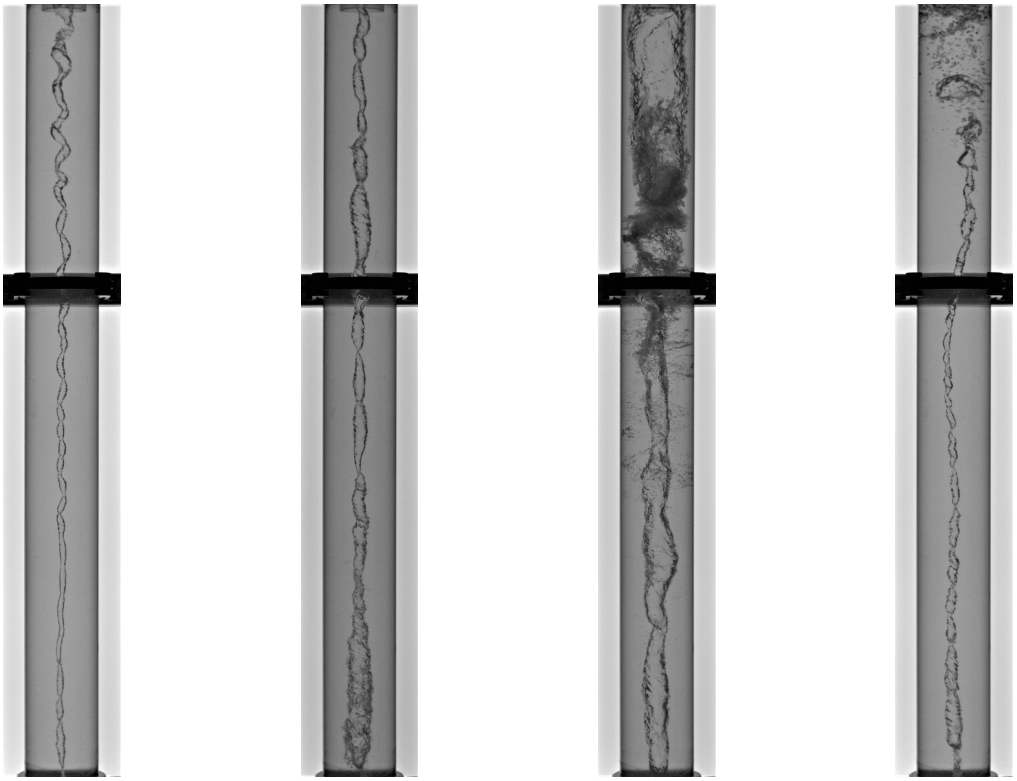

(a) (b) (c) (d)

Figure 2.4: Swirling gas liquid flow patterns, in the first figure a swirling gas column is presented. In the second figure a swirling intermittent flow is presented, a pulse can be seen entering from the bottom. The flow direction is from bottom to top and gravity points from top to bottom

was given equation 2.18, which states that after a critical core radius (R_c) the tangential velocity becomes constant. This equation was for single phase flows while this thesis deals with multiphase flows, therefore the gas core radius (R_g) is added in this equation so that it becomes

$$u_{\theta,l,0} = \begin{cases} 0 & \text{for } 0 < r < R_g \\ \frac{r}{R_c} u_{\theta,l,max} & \text{for } R_g \leq r < R_c \\ u_{\theta,l,max} & \text{for } R_c \leq r \leq R \end{cases} \tag{2.22}$$

In the situation that the gas core radius is larger than the critical core radius it is assumed that the u_θ profile is constant from the gas core to the wall such that the distribution becomes

$$u_{\theta,l,0} = \begin{cases} 0 & \text{for } 0 < r < R_g \\ u_{\theta,l,max} & \text{for } R_g \leq r \leq R \end{cases} \tag{2.23}$$

The tangential velocity is an important parameter for the total angular momentum flux. The total angular momentum flux is a conserved quantity so this can be used to determine u_θ in the pipeline after the swirl element. The angular momentum flux inside the swirl element can be approximated by

$$\dot{L}_{se} = \dot{m}_{tot} u_\theta (0.9 R_{se}) \tag{2.24}$$

Where $\dot{L}_{se}$ is the flux of angular momentum and $\dot{m}_{tot}$ is the combined mass flow of water and air, the $0.9R_{se}$ is the average radial position in the swirl element vanes. The visualisation for the $0.9R_{se}$ term is shown in Figure 2.5, where the average distance between the wall and the body is considered for multiplying the azimuthal velocity. The tangential velocity in the vanes can be approximated by $u_z \tan(\theta)$ as the water has to follow the vane direction. The total mass flow can be approximated by the mass flow of water as the mass of the air is negligible in comparison to that of water.

$$\dot{L}_{se} = \dot{m}_l u_{z,l,se} \tan(\theta) (0.9 R_{se}) \tag{2.25}$$

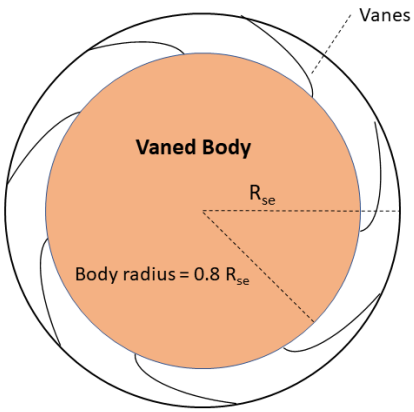

Figure 2.5: Sketch of the cross-section of the swirl elements used in this thesis. Important to note is the ratio of inner body radius to outer radius ratio of 0.8

$u_{z,l,se}$ is the liquid velocity in the swirl element, which is unknown. This will depend on the gas flow rate, since the areas occupied by the phases depends on the incoming flow rate of both gas and liquid. As angular momentum is a conserved quantity, the momentum generated in the swirl element should be the same as at the exit of the swirl element where the decay in this small section is neglected. The angular momentum in the liquid can be calculated by

$$\dot{L}_{pipe} = 2\pi \int_{R_g}^{R} \rho_l u_{z,pipe} u_{\theta,pipe} r^2 \, dr = \frac{2\pi}{3} \rho_l u_{z,pipe} u_{\theta,pipe} \left(R^3 - R_g^3\right) \tag{2.26}$$

$$\dot{L}_{pipe} = \frac{2}{3} \dot{m}_l u_{\theta,pipe} \frac{R^3 - R_g^3}{R^2 - R_g^2} \tag{2.27}$$

Where $\dot{L}_{pipe}$ is the angular momentum in the pipe, $u_{z,pipe}$ is the axial velocity in the pipe, $u_{\theta,pipe}$ is the angular velocity in the pipe. As mentioned, the flux of angular momentum has to be conserved, also shown in Figure 2.6, such that

$$\dot{L}_{se} = \dot{L}_{pipe} \tag{2.28}$$

By doing this the tangential velocity in the pipe can be obtained to be

$$\dot{m}_l u_{z,l,se} \tan(\theta) 0.9 R_{se} = \frac{2}{3} \dot{m}_l u_{\theta,pipe} \frac{R^3 - R_g^3}{R^2 - R_g^2} \tag{2.29}$$

$$u_{\theta,pipe} = 1.66 u_{z,l,se} \tan(\theta) \frac{R\left(\Delta R^2\right)}{\Delta R^3} \tag{2.30}$$

Here the $0.9R_{se}$ has been replaced by the pipe radius via $R_{se} = \frac{R}{0.814}$ and the ΔR^3 and ΔR^2 are the $R^3 - R_g^3$ and $R^2 - R_g^2$ terms respectively. As the axial velocity in the swirl element depends on the gas, some assumption has to be made in order to close the problem, this will be discussed in the next chapter. For convenience, $u_{\theta,pipe}$ will be referred to as u_θ for the remainder of this thesis.

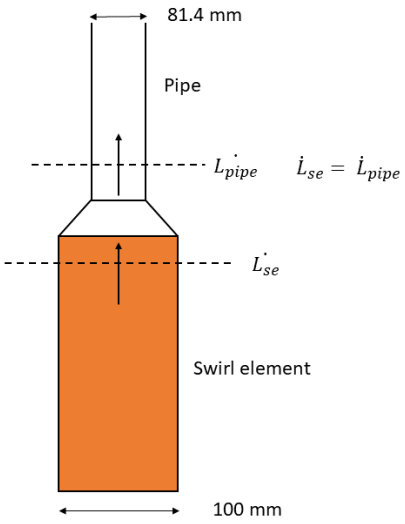

Figure 2.6: A sketch showing that the angular momentum flux generated in the swirl element is conserved and equal to the angular momentum flux in the pipe.

3

Towards a mechanistic model

One of the main goals of this thesis was to propose a mechanistic model which can determine the transition between regular flow patterns and flow patterns where a gas column is present in the centre of the pipe, the so called columnar or swirling patterns. The transition can be predicted either based on empirical flow regime maps or via a mechanistic model. For the latter an attempt will be made in this thesis.

3.1. Forces involved

Before a mechanistic can be constructed, the relevant forces have to be found. The reference situation will be one where bubbly flow is present. In Figure 3.1a a situation can be seen where there is no tangential velocity component and normal bubbly flow is present. If the flow is then brought in rotation, an u_θ will arise which

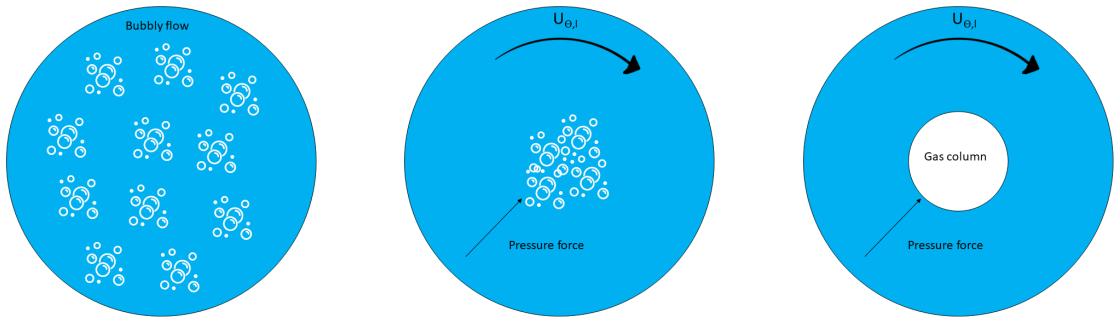

(a) (b) (c)

Figure 3.1: A sketch of the cross section for three situations, (a) where there is no tangential velocity, (b) where there is a tangential velocity and the column is forming and (c) where the gas column has formed if the tangential velocity is great enough

will then cause a radial pressure gradient according to equation 2.13. Due to the velocity profiles stated in equation 2.22, the radial pressure gradient will also change over the radius, as this is dependent on u_θ. Due to these velocity profiles, the pressure gradient will change in to

$$\frac{\partial p}{\partial r} = \begin{cases} \frac{\rho_l}{r}\left(u_{\theta,max}\frac{r}{R_c}\right)^2 = \rho_l u_{\theta,max}^2 \frac{r}{R_c^2} & \text{for} R_g < r < R_c \\ \rho_l \frac{u_{\theta,max}^2}{r} & \text{for} R_c \leq r \leq R \end{cases} \tag{3.1}$$

If the gas core radius is larger than the critical core radius then it will return the to form of 2.13, such that it becomes

$$\frac{\partial p}{\partial r} = \frac{\rho_l u_\theta^2}{r} \tag{3.2}$$

This can be used to calculate the pressure difference between the wall and air-water interface if a column has formed. The pressure difference between the wall and the interface is then calculated as

$$p(R) - p(R_g) = \int_{R_g}^{R_c} \rho_l u_{\theta,max}^2 \frac{r}{R_c^2}\, dr + \int_{R_c}^{R} \rho_l \frac{u_{\theta,max}^2}{r}\, dr \tag{3.3}$$

$$\Delta P(R_g, u_{\theta,max}) = \int_{R_g}^{R_c} \rho_l u_{\theta,max}^2 \frac{r}{R_c^2}\, dr + \int_{R_c}^{R} \rho_l \frac{u_{\theta,max}^2}{r}\, dr \tag{3.4}$$

Or, when the gas core radius is larger than the critical core radius

$$\Delta p(R_g, u_{\theta,max}) = \int_{R_g}^{R} \rho_l \frac{u_{\theta,max}}{r}\, dr \tag{3.5}$$

Where Δp is the pressure difference between the wall and the interface. When this pressure difference is large enough, the bubbles will start migrating towards the centre of the pipe, as shown in Figure 3.1b. When u_θ is then great enough the bubbles will coalesce and form a gas column in the middle of the pipe, as shown in figure 3.1c. From these equations it becomes clear that u_θ has a big influence on the formation of a gas column type flow.

3.2. Transition to columnar flow types for different upstream conditions

The case mentioned in the previous section was for bubbly flow upstream of the separator, where the formation of the column is determined by the pressure difference between the core and the wall. Bubbly flow is not the only flow type present as slug, churn and annular can also exist depending on the gas flow and liquid flow rates. However, for these flow types, the transition criteria based on bubbly flow can still work. The Taylor bubbles which are present in slug flow and the larger bubbles present in churn flow are generally already in the middle of the pipe and therefore do not have to be pushed towards the centre to form a gas column. The Taylor and larger bubbles will remain larger bubbles in the swirling section, this explains the behaviour of the pattern swirling burst as follows.

In slug or churn flows, there is an alternating pattern of large bubbles after which a section of liquid passes through, this can also be seen in Figure 3.2. When a large bubble passes through the swirl element, a larger core will appear in the swirling section. The liquid slugs, containing small bubbles, follow these larger gas bubbles. As there is a sudden transition from large gas bubbles to liquid slugs, the core will rapidly shrink in size when this transition passes through the swirl element. At this transition, either not all the bubbles are pushed to the centre, or bubbles appear due to the breakage of the core, this can also be seen in Figure 2.4c.

For the formation of a columnar type flow, the liquid speed should be high enough in order to generate the radial pressure gradient necessary to push all bubbles in the liquid towards the centre. This criteria will still be valid for slug and churn flows, because for the same flow rate of liquid, the water velocity will be equal or greater than that from bubbly flow. This indicates that all the bubbles in the liquid slugs will be pushed towards the centre, while the larger bubbles are already in the middle of the pipe as mentioned before. So by this reasoning, if a gas column forms for bubbly flow, it should also form if the incoming flow is slug or churn.

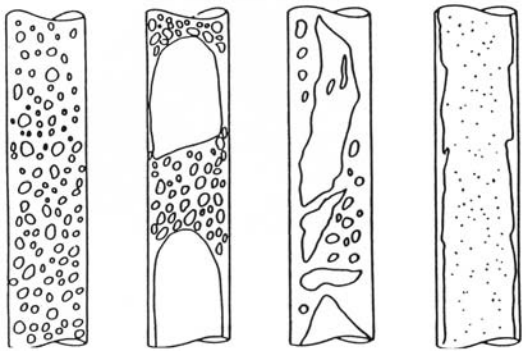

Figure 3.2: A sketch of bubbly, slug, churn and annular flow. Important here is to observe the bubble regions in between the Taylor bubbles and the larger bubbles within churn flow. Figure taken from [18]

There is however one uncertainty in this reasoning. In section 3.1, the transition was based on bubbly flow, such that at a certain Δp, a column would form in the middle of the pipe. Then the condition was set that for slug and churn flow only the bubbles in the liquid slugs have to be pushed to the centre. The result from this was, that for a certain flow rate of liquid, a column should form regardless of the upstream flow pattern, which could also be seen in Liu and Bai, Shakutsui et al.[8, 14–16]. It was not considered however that the liquid velocity in the slugs increases when the gas flow rate is increased.

An increase in liquid velocity, causes an increase in u_θ since the two quantities are linked by the angle of the swirl element vanes, such that the Δp would also increase. If the transition is dependent on a certain value for Δp, an increasing gas flow rate would result in a larger Δp. From this reasoning, it would then seem that the transition from non-columnar to columnar flow types could happen at a lower u_{sl} for larger values of u_{sg}. This is inconsistent with what is previously found in literature [8, 14–16] where a transition independent of u_{sg} was shown. A potential explanation lays within the gas core radius. The pressure difference is dependent on both u_θ and R_g. For slug and churn flow, a larger core will form as the void fraction of the incoming flow is larger. A larger core radius will result in a lower pressure difference. It is possible that these two effects of increasing u_θ and increasing R_g cancel each other out, such that at the transition the pressure difference is constant.

3.3. Estimation of the axial velocity in the swirl element

From the previous sections it can be concluded that u_θ is a very important parameter for the formation of a gas column. In Chapter 2.3 an equation was derived for u_θ in the pipe based on the conservation of angular momentum. In this equation there was still one unknown, the axial velocity of liquid inside the swirl element ($u_{z,se}$). This problem cannot be solved as the areas occupied by the gas and the liquid inside the swirl element are unknown. Some assumptions have to be made on the conditions inside the swirl element to be able to close this problem, as experiments to determine this were not performed during this thesis. For these assumptions the supplementary information of Liu and Bai [8] was used. In their experiments a swirl element which was inserted into a pipe with transparent walls, allowing to observe what happens inside the swirl element. From the videos provided in their supplementary information, it can be observed that the flow separation already occurs within the swirl element. Based on this two different models are proposed

3.3.1. Assumption based on annular flow

Because of the flow separation, the conditions might be very similar to that of annular flow as the air seems to be collected in the middle of the vane channel, From annular flow it is known that the pressure drop on the liquid side is the same as that on the gas side, such that both the friction factor and stresses should be similar. Therefore a ratio of velocities between the gas and liquid can be obtained as

$$f_i \rho_l u_{z,l,se}^2 = f_i \rho_g u_{z,g,se}^2 \tag{3.6}$$

$$\frac{u_{z,g,se}}{u_{z,l,se}} = \sqrt{\frac{\rho_l}{\rho_g}} \approx 28.8 \tag{3.7}$$

With the ratio of velocities known, the velocity of liquid inside the swirl element is connected to the liquid velocity in the swirl by equation 3.7 and can be calculated using the conservation of mass.

$$A_{pipe} u_{sl} = A_{l,se} u_{z,l,se} \tag{3.8}$$

$$u_{z,l,se} = u_{sl} \frac{A_{pipe}}{A_{se,l}} \tag{3.9}$$

Where A_{pipe} is the area of the pipe and $A_{l,se}$ is the area of the liquid in the swirl element. A similar thing can be done for gas, where the gas velocity in the swirl element is connected to the liquid velocity by $u_{z,g,se} = 28.8 u_{z,l,se}$

$$A_{pipe} u_{sg} = A_{g,se} 28.8 u_{z,l,se} \tag{3.10}$$

$$u_{z,l,se} = \frac{u_{sg}}{28.8} \frac{A_{pipe}}{A_{se,g}} \tag{3.11}$$

With two equations for $u_{z,l,se}$, either the gas or the liquid area inside the swirl element can then be eliminated, and the resulting equation can then be used together with the total area inside the swirl element to obtain the

liquid area inside the swirl based on u_{sg} and u_{sl}

$$A_{se,g} = A_{se,l}\frac{u_{sg}}{28.8u_{sl}} \tag{3.12}$$

$$A_{se} = A_{se,g} + A_{se,l} \tag{3.13}$$

$$A_{se,l} = \frac{A_{se}}{1+\frac{u_{sg}}{28.8u_{sl}}} \tag{3.14}$$

With the area of the liquid expressed with known parameters, the velocity of liquid inside the swirl element is given by:

$$u_{z,l,se} = u_{sl}\frac{A_{pipe}}{A_{se}}\left(1+\frac{u_{sg}}{28.8u_{sl}}\right) \tag{3.15}$$

With this velocity known u_θ can be calculated based on u_{sl}, u_{sg} and R_g according to:

$$u_{\theta,pipe} = 1.66u_{sl}\frac{A_{pipe}}{A_{se}}\tan(\theta)\frac{R(\Delta R^2)}{\Delta R^3}\left(1+\frac{u_{sg}}{28.8u_{sl}}\right) \tag{3.16}$$

The result of the assumption that annular flow is present in the swirl element is that u_θ will mostly depend on the core size radius for large liquid flow rates, but can be strongly effected by the gas flow rate for low liquid flow rates. This can be seen in the appendix D where plots of the $\frac{R(\Delta R^2)}{\Delta R^3}$ term, a plot of the $\left(1+\frac{u_{sg}}{30u_{sl}}\right)$ term with an u_{sl} of 0.1 $\mathrm{m\,s^{-1}}$ and a plot of the $\left(1+\frac{u_{sg}}{30u_{sl}}\right)$ term with an u_{sl} 0.5 are shown. The u_θ obtained via this equation should be taken with a grain of salt, as the assumption of annular flow in the swirl element is only based on a video and no actual measurements were performed.

3.3.2. Assumption based on core conditions

The second possible assumption is based on the core condition and the conditions in the swirl element being similar. The swirl in the liquid is already present at the edge of the vanes, while separation already occurs in the swirl element, such that void fraction in the vanes ($\alpha_{g,se}$) is better approximated by the void fraction of the core($\alpha_{g,core}$) than the homogeneous/upstream void fraction (α_g). The core void fraction is generally a lot lower than the homogeneous void fraction [8, 15, 16], a similar thing can be seen in the videos of the supplementary material of Liu and Bai[8], where the incoming gas is transformed to a tiny streak of gas such that the conditions in the core and swirl element are assumed to be similar. With this assumption, the area of the liquid can be extracted from the conservation of mass again.

$$A_{pipe}u_{sl} = A_{se,l}u_{z,l,se} \tag{3.17}$$

As before, the area of the liquid in the pipe can be expressed as a function of the total area in the swirl and the area of the gas inside the swirl

$$A_{pipe}u_{sl} = u_{z,l,se}(A_{se} - A_{g,se}) \tag{3.18}$$

The area of the gas is now a function of the void fraction downstream of the swirl element and the total area of the swirl element the velocity of the liquid inside the swirl becomes

$$A_{pipe}u_{sl} = u_{z,l,se}A_{se}(1-\alpha_{g,core})u_{z,l,se} = u_{sl}\frac{A_{pipe}}{A_{se}}\frac{1}{1-\alpha_{g,core}} \tag{3.19}$$

As the axial velocity in the swirl element can now be approximated based on superficial liquid velocity and gas core void fraction, the tangential velocity in the pipe can be approximated by

$$u_{\theta,pipe} = 1.66u_{sl}\frac{A_{pipe}}{A_{se}}\tan(\theta)\frac{R(\Delta R^2)}{\Delta R^3}\left(\frac{1}{1-\alpha_{g,core}}\right) \tag{3.20}$$

This equation for u_θ should just as the last one be taken with a grain of salt as the assumption that the gas core void fraction and the void fraction in the swirl element are similar is just based on the supplementary material provided by Liu and Bai[8]. Both of the models should be validated in the future as their was unfortunately no time to verify the assumptions made in this thesis both due to lack of time and the use of a non-transparent swirl element. With these equations an approximation for both the tangential velocity and pressure difference can be made both of which are shown in the next chapter.

3.4. Parameters yet to be investigated

The model developed in this chapter considered the transition from non-columnar flow patterns to be dependent on the pressure difference between the wall and the gas-liquid interface. The tangential velocity, which is necessary for calculating the pressure difference between the wall and the interface, was approximated by the conservation of angular momentum and the assumptions on the conditions inside the swirl element. This can be the start of a mechanistic model however, the influence of a lot of parameters is not yet known. In the setup used in this thesis, only 1 pipe diameter was present such that the influence of this could not be investigated. In the model it is also not yet present, for completion of the model the influence of the pipe diameter should be investigated. Other parameters such as the surface tension could also have and influence on the formation of the core, such that for a different surface tension, the core might form at a higher or lower u_{sl}. The velocity distributions used in this model were from a single phase flow, it is possible that for a gas-liquid system this distribution is different such that the pressure gradients would be different. A different pressure gradient results in a different pressure difference, so for an accurate description the tangential velocity profiles should be known. There is still a lot of unknowns however, due to time constraints these could not be investigated.

4

Experimental procedure

This chapter will give an description of all the experiment performed. It starts with a general overview of the set-up and covers the different types of equipment that were used. Together with the overview of the equipment used there is an description of the flow loop. After this it will be described how the flow regime maps were made and how the patterns were identified. The determination of the core size is also given while an indication of the errors present are also given.

4.1. Setup

4.1.1. Flow loop

The experiments performed in this thesis use a flow rig designed and build by Matheus Martinez Garcia (PhD candidate) and Evert Wagner (Lab Technician), present in the New Applied Science Building at Delft University of Technology . An general overview of the flow rig can be seen in figure 4.1. The flow rig consists of piping made of Poly Vinyl Chloride, a buffer vessel to store water, two settling tanks, valves, a swirl element, an air sparger, pumps and flow meters.

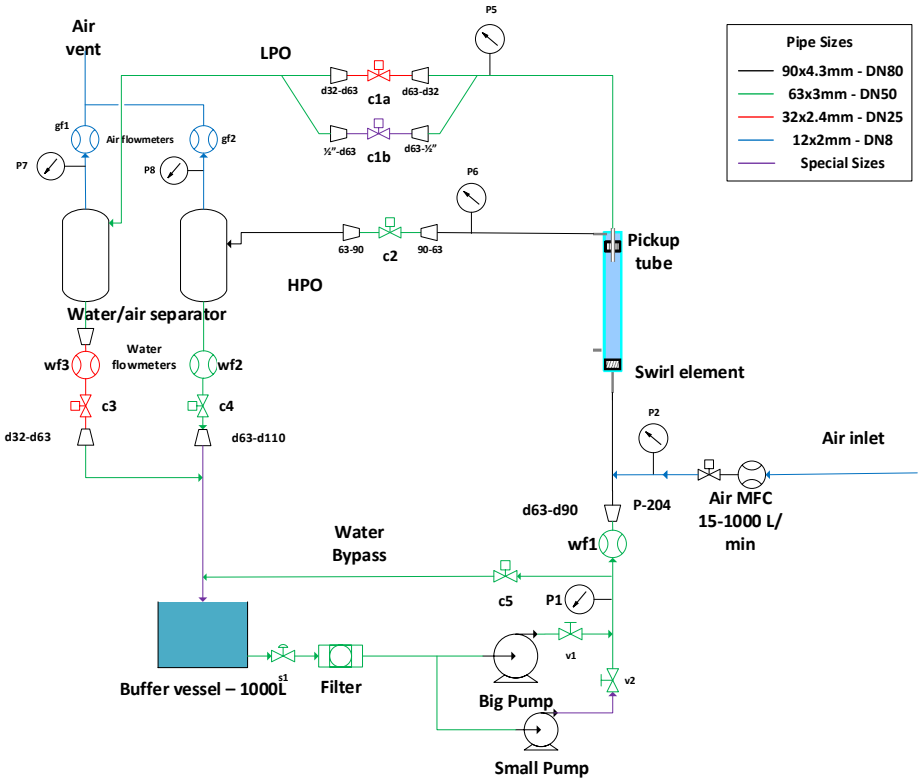

Figure 4.1: An overview of the setup used in this thesis

There are two pumps available for pumping water through the set up, the Iwaki Magnet Pump referred to in this thesis as the small pump and the Lowara HPSS50-250/220, referred to as the large pump. The water is pumped from a buffer vessel of 1000 L. After the pumps the pressure is measured by the pressure sensor which is indicated as p1, this is a PMP 5016-TA-A1-CA-HO-PJ model. The water is pumped upwards through PVC piping towards the swirl element. Shortly after the pump a bypass is present, with the bypass the lower flow rates can be achieved while still maintaining a high enough frequency for the pump. After the bypass, the diameter from the pipes expand from an inner diameter (ID) of 50 mm to 81.4 mm After the expansion, the flow from the pumps is measured by an electromagnetic flow meter, this flow meter is referred to as wf1, as seen in Figure 4.1. After the water flow is measured, air is injected via an in-house designed sparger which can deliver flow rates of 8 Ln/min up to 1000 Ln/min (normal liters per minute). The air flow is controlled by a Bronkhorst El-Flow Select Mass Flow Controller, that controls the mass flow rate of air after which it converts it to normal liters per minute based on the density of air at 0 °C and 1 atm.

The mixture of air and water flows through a section of 2.74 m ($\approx 33.7D$) before it reaches the swirl element to ensure that the flow is fully developed. The mixture then flows through a swirl element which brings the flow in to rotation. After the swirl element there is a section of 1.3 m of PVC pipe where the flow can be observed. At the end of the swirl section there are two outlets, the pickup tube (also referred to as Light Phase outlet (LPO)), which captures the lighter phase and the Heavy Phase Outlet (HPO), which captures the heavier phase. The flow split can be controlled using valves further downstream, however this was not within the interest of this thesis. The outlets lead to separate gravity tanks to fully separate the water and air. The air leaves the gravity tansk via the top part where the flow can be measured. The sensor which is connected to the gravity tank from the LPO is referred to as gf1 and the sensor which is connected to the other tank is referred to as gf2. The water leaves at the bottom of the gravity tanks where it first passes through a flow meter. After the water flow meters the water will flow back to the buffer vessel. Detailed information on the valves and flow meters that were not used in this thesis can be found in the setup manual[24].

4.1.2. Swirl element geometry

This thesis makes use of four axial swirl elements, which were previously designed by Slot and Van Campen [1, 23]. These swirl elements have the same geometry and differ only in the angle of the vanes. A schematic depiction of the different swirl elements can be seen in figure 4.2.The swirl elements will be referred to by a number of 1 to 4, with number one being the weakest swirl element and number four the strongest; an overview of their respective vane angles and swirl numbers can be seen in table 4.1. The swirl elements all have an inner diameter of 100 mm while the vaned body has a diameter of 80 mm, the length of the swirl element encasing is ≈ 0.30 m.

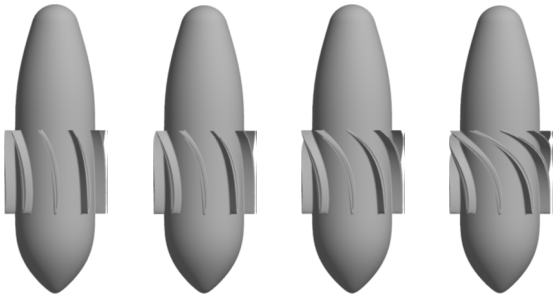

(a) 1 (b) 2 (c) 3 (d) 4

Figure 4.2: Schematic drawings of all the swirl elements, swirl element increases from left to right

Table 4.1: An overview of the swirl elements used with their respective vane angles and swirl numbers calculated according to equation 2.20

Swirl element indicator	**Vane angle Θ (°)**	**Swirl number**
1	40.2	1.72
2	51.5	2.56
3	63.1	4.01
4	73.0	6.67

4.1.3. Image capturing

In order to correctly identify the flow pattern present at any given flow rate of gas and liquid, a high speed camera is used. The camera, Basler acA1920-150uc, captures images which can be used to study the flow patterns present. This is necessary as it can be hard to distinguish the differences between flow patterns especially at the transition regions. On top of this, as the superficial velocities start increasing it can be difficult to observe what happens. Furthermore, the data provided by the cameras can be used to determine the void fraction and width of the swirling gas column. Two cameras are used in the thesis, one which captures footage from both upstream and downstream of the swirl element and one which is focused on the rest of the pipeline up to the pickup tube. Due to limitations of the software used, a maximum of 500 frames was captured for both cameras. Depending on the superficial velocity a frame rate of 50, 75 or 100 frames per second (fps) was used. This was for flow rates of water up to 0.3 m/s, from 0.3 to 0.5 m/s and from 0.5 m/s respectively. The water speed was chosen as a guideline as testing showed that this had the biggest influence on the ability to see what is happening.

A shutter time of 200 µs was used in order to reduce motion blur. Due to the low shutter time, an extra light source was needed. As a whole section of the set up was captured by the camera, an even distributed light source was needed. For these reasons led panels were chosen.

4.2. Flow pattern mapping

In this thesis flow pattern maps are constructed for three separate locations of the set up, these locations are just before the swirl element at z/D of 33.6 in relation to the sparger, where a region of around 0.20 m was used for observation, directly downstream of the swirl element where also a region of around 0.20 m was used for observation and close to the pick up tube where a region of around 0.34 m was used for observation. To clearly indicate where the observations for the different flow pattern were done an illustration is shown in Figure 4.3.

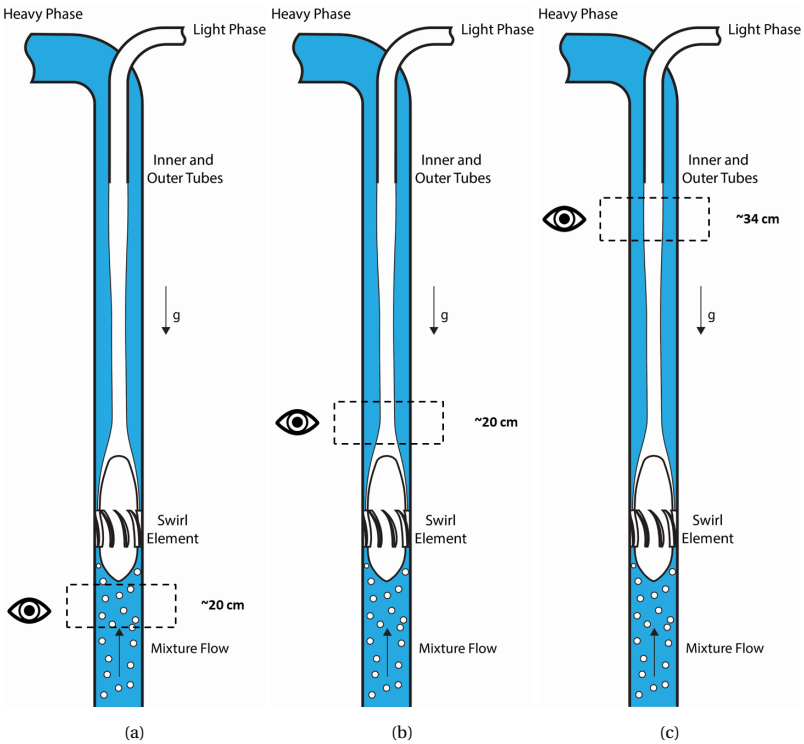

Figure 4.3: A visualisation of where the different maps were obtained, from left to right are the upstream, downstream and position at the pick up tube, the eyes roughly indicate where the observations were done. Original figures designed by Matheus Martinez Garcia.

To record all of the relevant flow rates and pressures, a custom Labview program designed by Matheus Martinez Garcia was used. With this program, the flow rates of both gas and liquids were recorded in Ln/min and Lmin^{-1} respectively and the pressure p1 which located just after the pumps in barg. All of these were recorded for 30 seconds at intervals of 0.5 seconds in order to get an average of the flow rates and pressure

p1. The superficial velocities of air and water were then calculated as:

$$u_{sl} = \frac{\phi_l}{60 \cdot 1000 \cdot A_{pipe}} \tag{4.1}$$

$$u_{sg} = \frac{\phi_g}{60 \cdot 1000 \cdot A_{pipe}} \tag{4.2}$$

In this equation u_{sl} and u_{sg} are the superficial gas and liquid velocities, ϕ_i is the respective flow rate in $\mathrm{L\,min^{-1}}$ or Ln/min and A_{pipe} is the cross-sectional area of the pipeline. The superficial gas velocity calculated from equation 4.2 still needs to be corrected for pressure and temperature as the normal liter is defined at 1 atmosphere and 237.15 °C. The correction is done using the following equation

$$u_{sg} = u_{sg} \frac{1.03125}{p_{1,avg} - 0.07 + 1.01325} \frac{293.15}{273.15} \tag{4.3}$$

In this equation the first fraction is to correct the flow rate based on pressure, the reason for this is that a normal litre per minute is defined at 1 atm, 273.15 K. The -0.07 bar term is account for the elevation losses of p1 up until the sparger. The second term is to correct the air speed based on the temperature difference at which the normal litre is defined and the temperature in the lab. The temperature in the lab was not measured but was assumed to be 20 °C as it is kept at this temperature by the building air conditioning. For the liquid, a range of around $10\,\mathrm{L\,min^{-1}}$ to $220\,\mathrm{L\,min^{-1}}$ was available. The reason for the upper limit was a combination of cavitation and air recycling in the system. With a flow of $250\,\mathrm{L\,min^{-1}}$, cavitation starts to form in the filter. However, for a flow rate of 300 Ln/min of gas and 220 Ln/min of water, the air started to be recycled in the water buffer. This prevented the liquid flow rate from going any higher. This range of flow rates gives a range in the superficial liquid velocity of around $0.03\,\mathrm{m\,s^{-1}}$ to $0.70\,\mathrm{m\,s^{-1}}$.

The air MFC can measure between 8 Ln/min to 1000 Ln/min, however since the behaviour did not change above 300 Ln/min, this value was taken as the limit for experiments done in this thesis. This yields roughly a range for u_{sg} of $0.02\,\mathrm{m\,s^{-1}}$ to $1.00\,\mathrm{m\,s^{-1}}$.

The patterns upstream the swirl element were categorised as bubbly, slug and churn. For the downstream patterns there were bubbly, slug and churn for the regular patterns and swirling column, swirling pulsating and swirling burst for the columnar flow patterns. As mentioned, the criteria for any columnar pattern was that it has to reach at least the first flange, around 20 cm away from the swirl element. The distinction made between the patterns swirling column and swirling pulsating lies in the intensity of the pulsations and the frequency. When a column starts pulsating a lot with pulsations that are relatively large to the average column, the pattern was regarded as swirling pulsating. The criteria to distinct the patterns swirling pulsating and swirling burst relies mainly on the appearance of the column and the presence of bubbles. If there are sudden contractions in the size of the column, usually accompanied with the presence of small bubbles, the pattern would be recorded as swirling burst.

At the pickup tube the same patterns could be chosen as those from the downstream region with the addition of the pattern swirl dying. For a columnar flow pattern to be present, it has to reach the pick up tube. The criteria to distinguish the columnar flow patterns is the same as before. For a pattern to be regarded as swirl dying, it has to have a column up until the last stabilising ring, 34 cm before the pick up tube. A trace of the column should still be visible though it has fallen apart in larger bubbles.

4.3. Core size determination

To determine u_θ based on equations 3.16 and 3.20, the gas void fraction of the core is needed. When identifying the patterns, the images that were captured had to be processed to determine the core diameter. This is done using Matlab with a code written by Matheus Martinez Garcia. The code first changes the figure from RGB to grayscale using the function *rgb2gray()*. After this the figure is cropped in both the radial and axial direction, for the radial direction the centre line of the gas column and the radius had to be manually determined. For the axial direction, a range of 600 pixels was chosen. The reason for this was that the figures were not that clear, which could cause the code to misidentify the borders of the gas column, the pipe wall also scatters light, which causes further misidentification of the core. This range was roughly from around 40 cm to 70 cm downstream of the swirl element. By taking a relatively large window of visualisation, the over- and underestimations of these errors could dampen each other which then results in a better estimation of the core. An example of these steps can be seen in Figure 4.4a

After these steps the contrast was enhanced using the function *imadjust()*to improve the boundary of between the gas core and the liquid surrounding it. After the contrast is enhanced, the figure is changed from grayscale to binary scale using the function *imbinarize()* where the water will be black and the air white. For this conversion a certain threshold is chosen to decide if the pixel will be black or white, in this thesis a value of 0.2 was chosen for swirl elements 2-4, 0.1 was used for swirl element 1 due to the lower quality of the core. Complementary to this threshold, a sliding window was used to filter out noise caused by small bubbles, a window of 2 X 2 was used. The results of these steps are shown in Figure 4.4b. With the binary image the core size can be determined by locating the interfaces on both size and determining the number of pixels between these interfaces. To calculate a core size from this, the ratio of pixels per unit of distance is needed. This is determined using the software ImageJ and the outer diameter of the pipe which is 90 mm. By measuring the outer diameter of the pipe in pixels and comparing it to the real value of 90, a conversion factor of 2.094 pixels per mm was found. from this it is determined that the scale is 2.094 pixels per mm. An example of the traced core is shown in Figure 4.4c. Since the pipe used is circular, refraction will make the core look bigger in the images than it in reality is, this should be corrected. The reason for this is that the light bends differently in water, air and PVC in such a way that the core appears bigger. The refraction indices of air, water and PVC are shown in table 4.2. A detailed description on how the core size is corrected can be found in the paper of Sattar et al. [25].

Table 4.2: Refraction indices of the various components present in the system, values taken from [26, 27]

Component	**Refraction index**
Air	1.000
PVC	1.531
Water	1.333

With the correction applied, the gas diameter can be found for every pixel in the axial direction after which the average gas core diameter of the figure is calculated. With the average core diameter of the figure known, the void fraction of the gas column can then be calculated according to equation 4.4 where D_{core} is the average gas core diameter.

$$\alpha_{g,core} = \frac{D_{core}^2}{D_{pipe}^2} \tag{4.4}$$

The gas core radius which is needed in both equations 3.16 and 3.20 can be calculated from the core void fraction according to

$$R_g = \sqrt{\alpha_g R^2} \tag{4.5}$$

4.4. Error propagation

The components which are most important for the error propagation are the flow sensors of water and air as these provide the bulk of the data used in this thesis and the pressure sensor p1 as this is used to correct the flow of air and the pipelines as they are used to calculate the superficial velocity of air. The water entering the flow loop is measured with an accuracy of $\pm(0.3\% m.v. + 0.12 L/min)$ where m.v. is the measured value. For the range used in this thesis, which is around $10-220$ L/min, this gives an error of $\pm$ 0.03 $\mathrm{L\,min^{-1}}$ to 0.66 $\mathrm{L\,min^{-1}}$. This means that the error in the water flow rate will be between 0.15 $\mathrm{L\,min^{-1}}$ to 0.78 $\mathrm{L\,min^{-1}}$, for u_{sl} this translates into 5×10^{-4} $\mathrm{m\,s^{-1}}$ to 2×10^{-3} $\mathrm{m\,s^{-1}}$.

The air flow entering the system is controlled via Bronkhorst Mass Flow controller with a range between 20 Ln/min to 1000 Ln/min. The error of this mass flow controller is $\pm(0.5\% m.v + 1 Ln/min)$, the first part of this error ranges from 0.040 Ln/min to 1.5 Ln/min. With the constant error added to this, the total error in the air flow rate ranges from 1.04 Ln/min to 2.5 Ln/min. This means that the uncorrected u_{sg} has an error in the range from 3×10^{-3} $\mathrm{m\,s^{-1}}$ to 8×10^{-3} $\mathrm{m\,s^{-1}}$. The pressure sensor has an uncertainty of $\pm$0.01 bar

Apart from the systematic error present due to the measurements, there is also a statistical error present as u_{sg} and u_{sl} are average values of the parameters. From the data gathered the mean and the sample variance can be calculated. The sample variance can be used to obtain the standard deviation, which can then be used to determine the 95% confidence interval around the averaged points according to

$$\bar{X}_n \pm t_{\alpha,n-1}\frac{S_n}{\sqrt{n}} \tag{4.6}$$

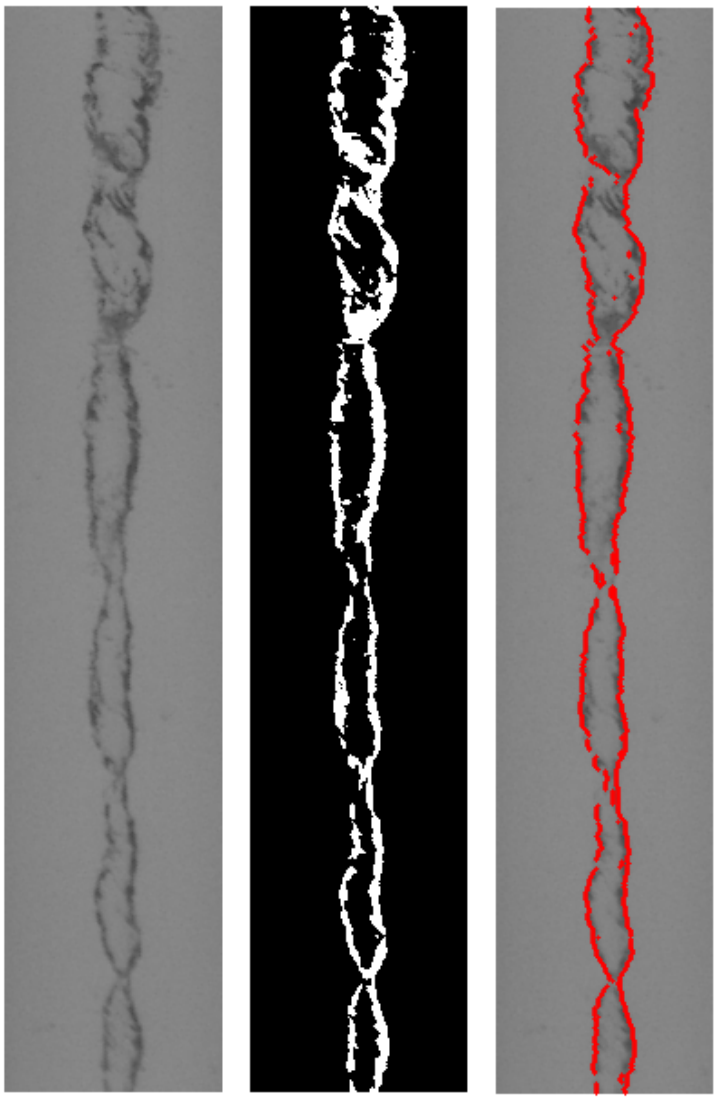

(a) (b) (c)

Figure 4.4: Image processing to determine the core size, the example used here is from swirl element 3 with $u_{sl} = 0.25\,\mathrm{m\,s^{-1}}$ and $u_{sg} = 0.042\,\mathrm{m\,s^{-1}}$. In the figure a, the cropped, greyscale image can be seen, in figure b, the binarized figure is shown. In figure c, the traced core can be observed where it plotted together with the original image

Where $t_{\alpha,n-1}$ is the t-value and S_n is the standard deviation. The t-value can be found in tables, the value used here is taken from $N-1=60$, which is 2.00.

The air superficial velocity is also corrected by using the pressure and temperature. For the temperature the assumption was made that the temperature of the lab was roughly constant at 20 °C based on the thermometer in the lab, which has an error of ± 0.5 °C. This does not have an indication for the error, for this reason this is also not included in the error calculation. The error for the corrected u_{sg} is calculated by

$$\sigma_{usg} = u_{sg}\sqrt{\left(\frac{\delta u_{sg}}{u_{sg}}\right)^2 + \left(\frac{\delta p1}{p1}\right)^2 + \left(\frac{\delta T}{T}\right)^2} \tag{4.7}$$

Where δu_{sg} and $\delta p1$ are the errors in the superficial gas velocity and pressure. To obtain the true error this has to be done for both the statistical and the random error. To obtain the true error in the corrected superficial gas velocity the errors should be added together. According to Taylor [28] this can be done in the following way.

$$\delta(u_{sg})_{total} = \sqrt{(\delta u_{sg,random})^2 + (\delta u_{sg,stat})^2} \tag{4.8}$$

Where $\delta u_{sg,tot}$ is the total error in the corrected u_{sg}, $\delta u_{sg,random}$ is the random error and $\delta u_{sg,stat}$ is the statistical error.

The error within the superficial velocities will most likely not be the largest error in the construction of the flow regime maps. The largest error will originate from the criteria and determination of the flow patterns. The patterns are determined via visual observation with the help of high speed cameras and the criteria for each flow pattern set in the previous section (4.2). Even though the criteria are set and high speed cameras are used, the determination of the patterns still gives rise to the largest error, as there is not a quantative criteria for the distinction between the columnar flow patterns. This means that distinguishing the difference between swirling column and swirling pulsating can change between experiments, leading to an uncertainty in the determination of flow patterns. Furthermore, the transitions between flow patterns are not sharp but continuous, such that they lead to a transitions region rather than a transition line.

5

Results and Discussion

In this chapter the results of the experiments are presented. First the various flow pattern maps for the three positions are shown. After that the transition from non-columnar to columnar flow types is discussed for the positions close to the swirl element and further away from the swirl element. The transitions within the columnar region are discussed after this and finally the model proposed in this thesis is compared to data found in literature.

5.1. Flow pattern maps

5.1.1. Flow regime map upstream the swirl element

In this section the results from the experiments are shown in the form of flow pattern maps. As mentioned in Chapter 4, there is a total of 3 flow pattern maps for each swirl element. As the maps upstream of the swirl element should all be the same regardless of the swirl element used, they have been plotted in a single figure which is Figure 5.1. In Figure 5.1 only the transition lines of the bubbly-slug and slug-churn transitions are present, calculated by 2.7 and 2.11. The remaining patterns are not observed for the flow rates considered in this thesis. When comparing the data obtained in this thesis to the transition lines given by Taitel et al.[19], one can observe that both the lines divide the regions relatively well. According to Figure 5.1, although the slug-churn transition is well captured by the model of Taitel et al.[19], a relatively big region of slug flow is presented where the bubbly flow is expected. This is expected however as the modelled transitions and observations done are never fully accurate and some points can end up on the wrong site of the transition. Close to the transition the patterns look very similar such that distinguishing them from each other can be quite difficult, this also induces and error in the visual observation. Furthermore, the patterns were taken after quite some elevation such that the pressure would be lower, which would then increase u_{sg} and shift the points towards the right causing better agreement with the modelled line. Another possible cause may originate form the sparger, only one sparger was used. By using a different sparger, smaller or larger bubbles can be created which can then result in less or more coalescence taking place.

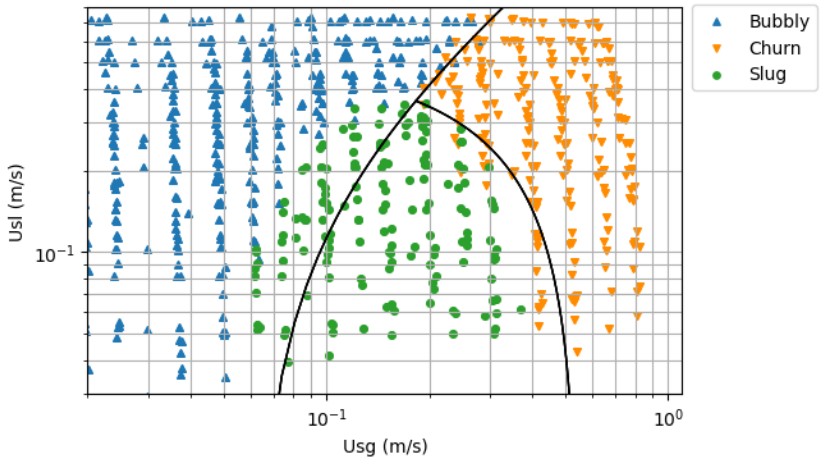

Figure 5.1: Flow pattern map upstream of the swirl element, the point identified experimentally are presented in colours, the black lines represent the transitions following the model proposed by Taitel et al.[19] (equations 2.8 and 2.11

5.1.2. Flow regime maps close to the swirl element

To clearly show the influence of the different swirl elements on the flow regime maps, those of swirl element 1 (the weakest) and 4 (the strongest) are shown in Figure 5.3, the maps of swirl elements 2 and 3 are shown in appendix C.

In these figures it can be observed that the transition from the non-columnar flow patterns to the columnar flow patterns is a horizontal line. This indicates that the transition from non-columnar to columnar flow patterns is independent of the gas rate. When comparing the two maps to each other, it can be observed that this transition from non-columnar to columnar flow patterns happens at a different u_{sl}. This is expected due to the different swirl intensities generated by the swirl elements. From these maps it appears that the columnar flow types appear after a certain threshold value for u_{sl}, which depends on the strength of the swirl element used.

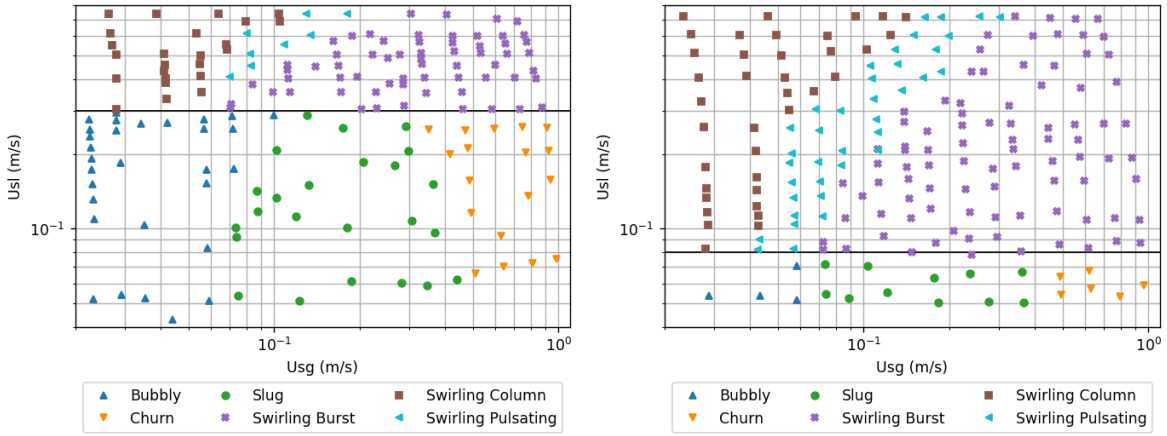

Figure 5.2: Flow regime maps of swirl elements 1 and 4. The black line indicates the transition from non-columnar flow patterns to columnar flow patterns.

In both of the maps in Figure 5.2, a swirling version of the classical flow patterns appears below the transition line. Above the transition line, the columnar flow patterns defined in chapter 2.2.4 appear which are swirling column(brown square), swirling pulsating (light blue triangle) and swirling burst (purple star).

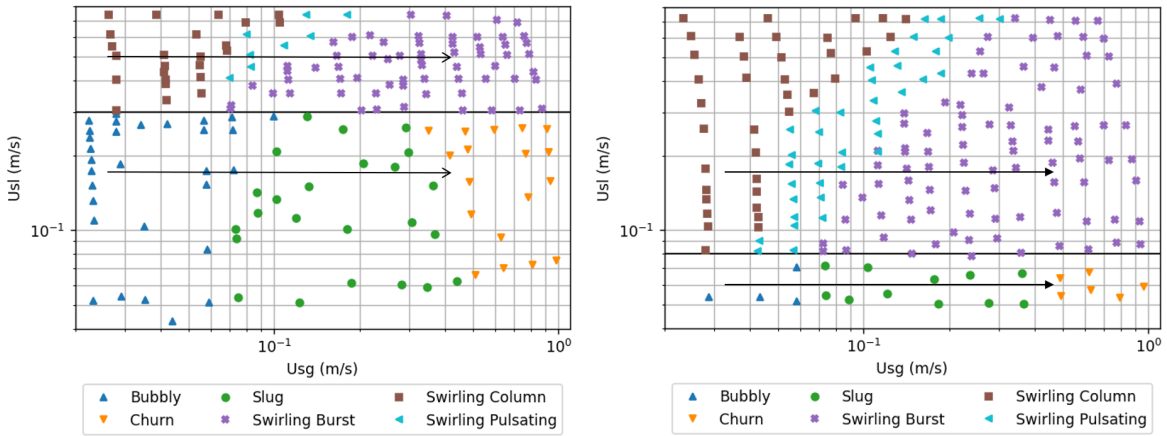

Figure 5.3: Flow pattern maps of swirl element 1 and 4 downstream of the swirl elements, the horizontal line represents the boundary between non-columnar and columnar flow patterns, arrow included is referred to in the text for more clarity, versions without the arrow can be found in appendix C

To see how the patterns change when either increasing the gas flow rate or the liquid flow rate, the maps are shown with a set of arrows plotted in them. Starting at a low flow rate of liquid, the lower arrow in Figure

5.3a and 5.3b, while the gas flow rate is also low, a swirling version of the pattern bubbly is present. Increasing the gas flow rate then yields swirling versions of the patterns slug and churn. Even though the transition to annular flow happens at lower gas flow rates for swirling flows [8], it is not seen in the range used in this thesis.

Starting from the same position as before, the pattern bubbly flow is present, when u_{sl} is then increased from its starting position while keeping the gas flow rate constant the patterns introduced in chapter 2.2.4 appear after a certain threshold value as mentioned before. If a high enough liquid flow is reached to form a columnar flow, the influence of the gas flow rate on the patterns can be investigated again. This is indicated by the higher arrows in Figure 5.3. Following the arrow, thus increasing u_{sg} yields the pattern swirling pulsating. The pulsating seems to be connected to what happens upstream of the swirl element. When the flow upstream is transitioning from bubbly to slug flow, larger bubbles will already start appearing which result in a pulse after it travels through the swirl element. An example of this can be seen in Figure 5.4, here a number of images are shown where in the first a larger bubble can be seen in the section before the swirl element. By Figure 5.4c this bubble has fully entered the swirl element. It can then be calculated after how many frames the pulsation should appear after first entering the swirl element based on the known velocity. To calculate the number of frames, the gas area in the swirl is neglected such that only the liquid rate is of importance. This follows the same reasoning as in chapter 3. With this assumption the speed in the swirl element can be approximated by $u_{sl}\frac{A_{pipe}}{A_{se}} = u_{z,se}$. The ratio of areas can be calculated such that the relation between the velocities is $1.84u_{sl} = u_{z,se}$. With the length of the swirl element known, the time it takes to travel through the swirl element can simply be calculated to be 0.41 s. In between Figure 5.4b and 5.4e there are around 0.35-0.41 s depending on which image is chosen as the starting point confirming that what happens upstream is related to what happens downstream. This is also in line with what has been found by Liu and Bai[8], where they showed that a Taylor bubbles travelling through the swirl element result in an expansion downstream.

By further increasing u_{sg}, the flow pattern transitions from swirling pulsating to swirling burst. Similarly to the swirling pulsating, the bursts are connected to what happens upstream of the swirl element. The swirling burst pattern seems to appear when the upstream pattern is either slug or churn flow, the exception to this is swirl element 1. A possible reason for this is that the swirl created by this element is too weak to keep the core intact when a larger bubble comes through. This then results in a more chaotic flow where smaller bubbles are dispersed through the liquid as a result of the column breaking. Swirling burst then appears for the remainder of the range used in this thesis. A potential cause for the link between the swirling burst pattern downstream and slug or churn patterns upstream is due to the nature of this respective flows. These flow types show alternating flow rates of gas and liquid when a one cross-section of the pipe is observed. When a Taylor bubble passes through, there will almost be no flow of water. If such a Taylor bubble then passes through the swirl element, there will be almost no water present to generate centripetal forces such that it only slightly compresses and gaps or sudden contractions can appear when the liquid slug then follows it. This is inline with the definition from chapter 2.2.4.

When comparing the flow pattern maps of swirl elements 1 and 4 some similarities and differences can be observed. Both the maps show the regular flow patterns and the swirling flow patterns introduced in this thesis (except for swirl dying that takes place close to the pick up tube). Furthermore, both of the maps show a transition between the patterns with and without a column (those with the swirling adjective) to be independent of u_{sg} in the range used in this thesis. Results from literature show a similar trend up until the annular region [8, 14]. This transition does take place at different superficial velocities depending on the swirl element used. For swirl element 1, the transition happens at an u_{sl} of $0.30\,\mathrm{m\,s^{-1}}$ while for swirl element 4 the transition happens at an u_{sl} of $0.08\,\mathrm{m\,s^{-1}}$. This is expected as swirl element 4 generates a larger swirl number as shown in 4.1 which indicates that for a similar axial velocity the intensity of the generated swirl will be higher.

5.1.3. Flow regime maps close to pick up tube

As the swirl number decays over the length of the pipe, and thus the centripetal effects needed to generate a core, the influence of the swirl number in the transition to columnar regimes can be investigated by analysing the flow close to the pick up tube. Once again the maps of 1 and 4 are taken to clearly show the difference between the different swirl elements, these are plotted in Figure 5.5. Comparing these maps to those close to the outlet of the swirl elements, similarities and differences can be observed. In both of the maps the classical flow patterns appear again. The region where they are present is now larger though which can be attributed to the decay of u_θ. The columnar flow patterns are also present again though the transition now happens at a higher u_{sl} due to the decay of u_θ. In between these regions there is now a transition region where the pattern introduced in this thesis, swirl dying, starts appearing.

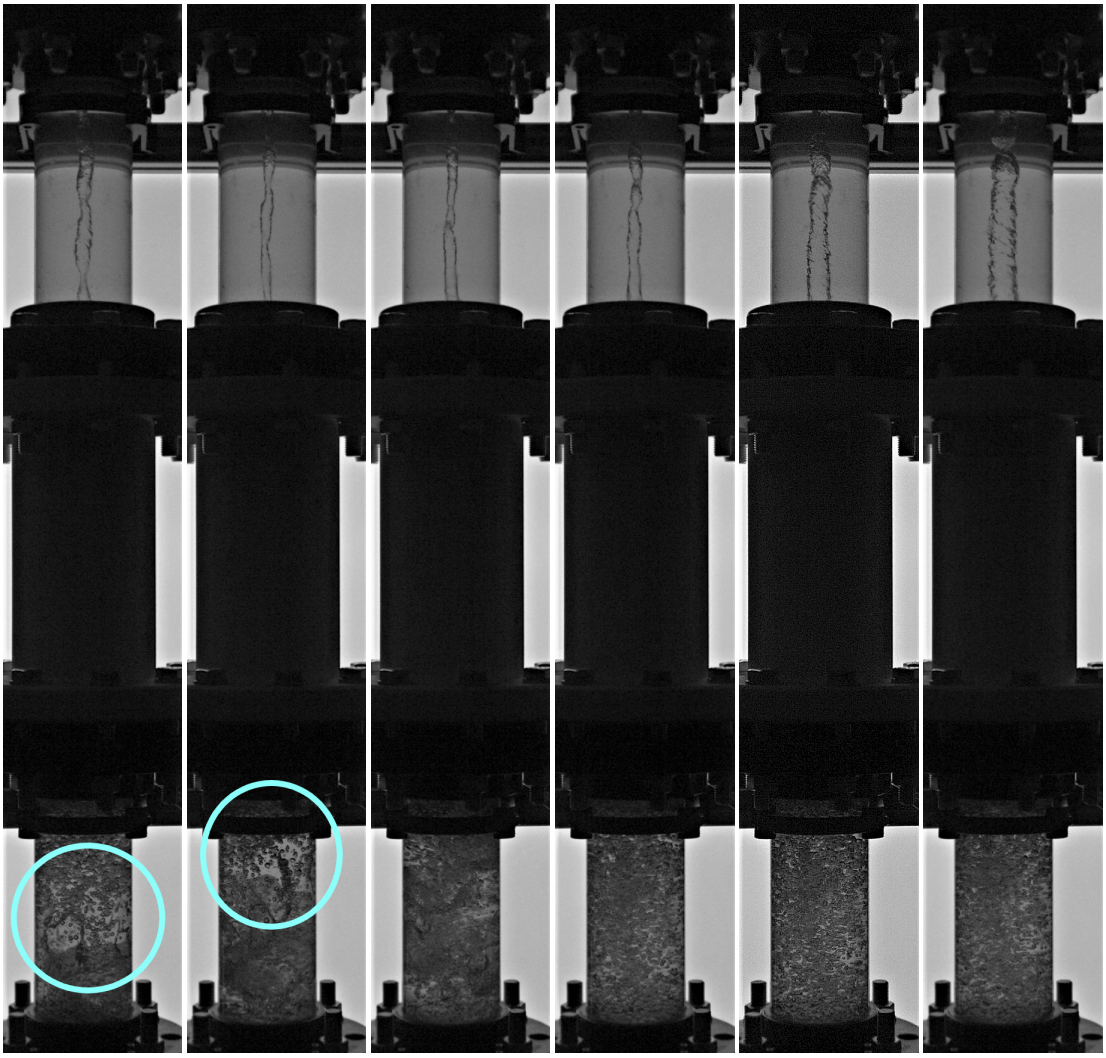

(a) $t = 0.0\,\mathrm{s}$ (b) $t = 0.07\,\mathrm{s}$ (c) $t = 0.17\,\mathrm{s}$ (d) $t = 0.47\,\mathrm{s}$ (e) $t = 0.48\,\mathrm{s}$ (f) $t = 0.49\,\mathrm{s}$

Figure 5.4: A sequence of photographs which show the influence of the upstream conditions. A larger bubble can be seen coming through in a, in figure b the tip has entered the swirl element, by photo c it has fully entered the swirl element, a skip of 22 frames later the larger bubble comes through as a pulse in the latter photographs. The flow direction is upwards while gravity points downwards, swirl element 3 is used here with an u_{sl} of $0.40\,\mathrm{m\,s^{-1}}$ and an u_{sg} of $0.11\,\mathrm{m\,s^{-1}}$

In the flow pattern maps close to the swirl element, the transition from non-columnar flow patterns to columnar flow patterns was independent of the gas flow rate. This was not the case for the flow regime maps close to the pick up tube, a dependency on the gas flow rate can be observed, especially in Figure 5.5b. A possible reason for this is that the increase in gas flow rate causes a thinner layer of liquid to form, this then increases the shear on the wall causing u_θ to decay faster which is similar to the reasoning of Shakutsui et al. [15]. A visualisation of this is shown in Figure 5.6 and also indicated with an arrow of the path taken in Figure 5.5b, where there is a constant u_{sl} and u_{sg} is increased from the left to the right. The sequence of figures starts with swirl pulsating at the most left figure (5.6a) which transforms into swirling burst which is represented by Figures 5.6b and 5.6c. Further increasing u_{sg} the flow transitions in to swirl dying, represented by Figures 5.6d and 5.6e. Further increasing the gas flow rate results in a regular flow pattern which in this case is churn flow, represented by Figure 5.6f.

When comparing the maps to each other it can be observed that the map of swirl element 1 contains almost no swirling pulsating, while the map of element 4 has a reasonably large region. As mentioned in the previous section this most likely originates from a combination of the weaker swirl generated by element 1 together with the definition of the patterns, the decay of u_θ then plays an additional role in weakening the swirl causing almost no swirling pulsating to be present in the map of element 1.

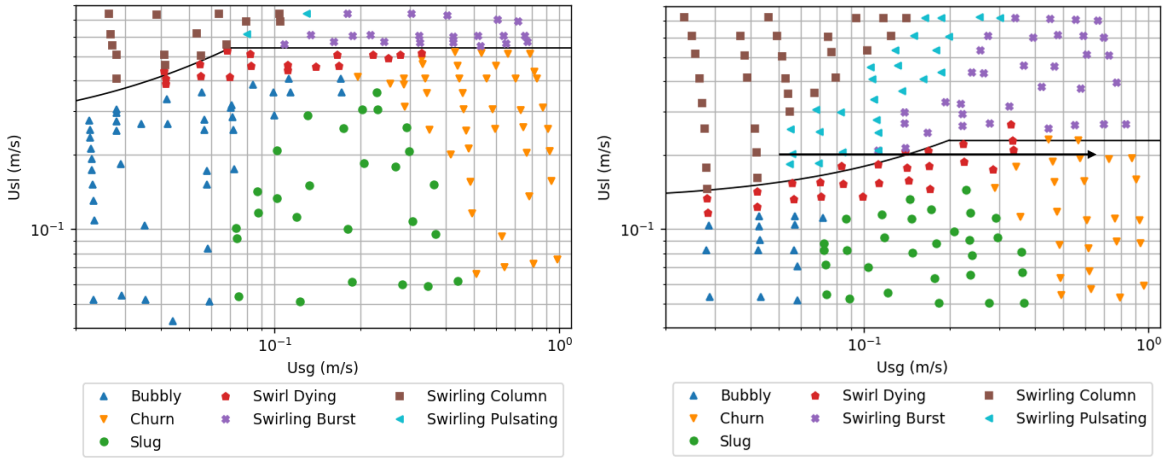

Figure 5.5: Flow pattern maps of swirl elements 1 (left) and 4 (right) near the pick up tube. The lines separates the non-columnar flows from the columnar flows where swirl dying is regarded as a non columnar flow. The arrow follows the transition from columnar flow types to non-columnar flow types as discussed in the text

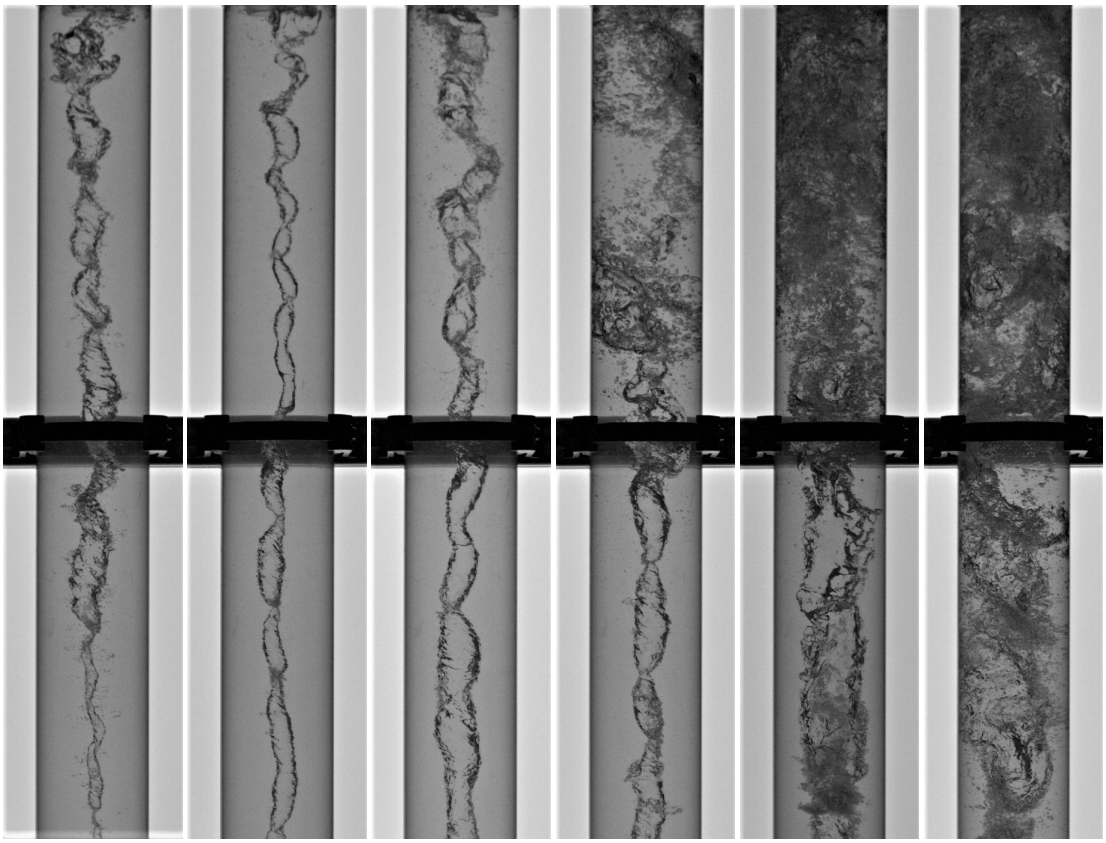

(a) 0.055 $\mathrm{m\,s^{-1}}$ (b) 0.11 $\mathrm{m\,s^{-1}}$ (c) 0.14 $\mathrm{m\,s^{-1}}$ (d) 0.17 $\mathrm{m\,s^{-1}}$ (e) 0.33 $\mathrm{m\,s^{-1}}$ (f) 0.56 $\mathrm{m\,s^{-1}}$

Figure 5.6: Influence of gas flow rate on flow patterns close to the pick up tube, constant $u_{sl} = 0.20\,\mathrm{m\,s^{-1}}$ with u_{sg} increasing from the left to right: 0.055, 0.11, 0.14, 0.17, 0.33, 0.56 $\mathrm{m\,s^{-1}}$, which is also indicated below each figure. From left to right, the pattern changes from swirling pulsating (a-c) to swirl dying (c-d) and finally churn flow (e). Images taken while using swirl element 4

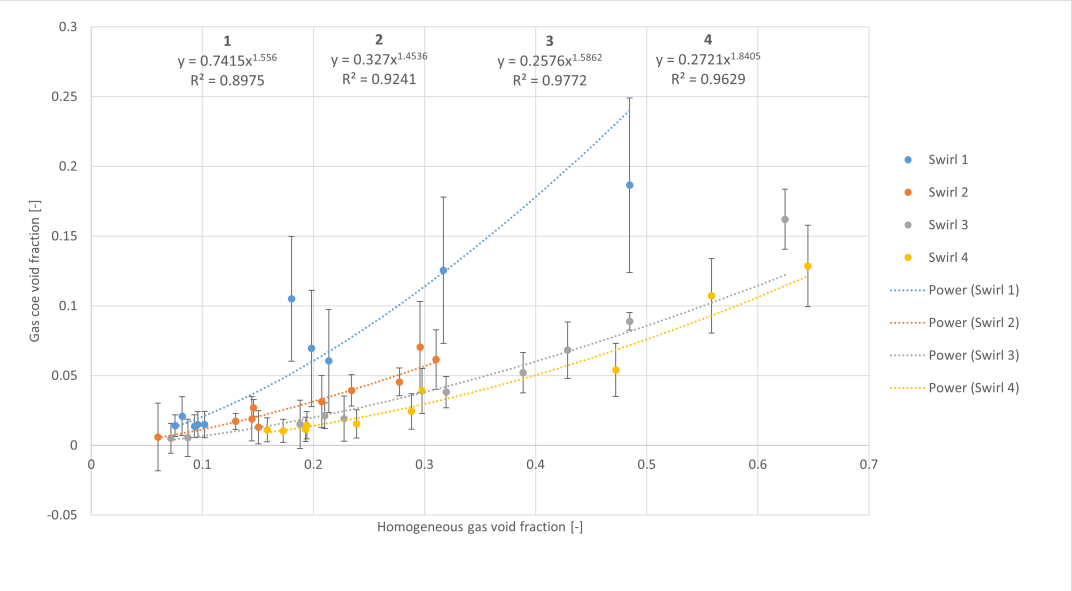

Figure 5.7: Plot of the homogeneous void fraction versus the core void fraction for every swirl element, the trendline which is a power law is plotted together with the respective equations and R^2 values. At the top the respective equations for the swirl elements are shown in order of swirl element 1-4. The error bars are the standard deviations from the core size and not the uncertainty of the fit

5.2. Transition from non-columnar to columnar flow patterns

5.2.1. Core void fraction

According to equations 3.16 and 3.20, u_θ is dependent on the void fraction and core size. Both of these can be obtained by the image processing procedure as described in chapter 4.3. These could not be done for every point as there was not camera footage taken for every point. The reason for this was that the camera footage was originally used to more accurately determine the transitions between flow regimes and therefore not taken for every point. Another consequence of this was that the images captured were not ideal for the determination of the core size, as the border between the liquid and the gas column was not always that sharp.

For every swirl element around 10 points were analysed for their void fractions. From this, the gas core radius can be calculated with equation 4.5. Via curve fitting, a relation between the homogeneous gas void fraction upstream and the core void fraction downstream of the swirl element. From this the core void fraction can be estimated based on the upstream conditions. The curve fit of all the different swirl elements is shown in Figure 5.7. The four swirl elements all produce a slightly different relation between the homogeneous void fraction and the core void fraction. Ordered from 1 to 4 the relations are

$$\alpha_{g,core} = \begin{cases} 0.742\alpha_g^{1.56} & \text{for swirl element 1} \\ 0.327\alpha_g^{1.45} & \text{for swirl element 2} \\ 0.258\alpha_g^{1.59} & \text{for swirl element 3} \\ 0.272\alpha_g^{1.84} & \text{for swirl element 4} \end{cases} \tag{5.1}$$

Where α_g is the homogeneous gas void fraction calculated according to equation 2.2. It should be noted that these equations are empirical relations and are only valid for the setup and void fractions used in this thesis. From Figure 5.7, it can be observed that a stronger swirl element generates a lower gas core void fraction for a similar homogeneous void fraction. For similar conditions, a stronger swirl element will produce a stronger centripetal force resulting in a smaller core. Another important observation is that the core void fraction is much smaller than the homogeneous void fraction, which results in a large gas velocity inside the core due to the conservation of mass. The core velocity roughly ranges from 2 to 10 $\mathrm{m\,s^{-1}}$, with an average of 4.5 $\mathrm{m\,s^{-1}}$ for all the swirl elements with the exception of swirl element 1, which is closer to 3 $\mathrm{m\,s^{-1}}$. A pos-

sible reason for this is that the cores formed by swirl element 1 were generally more unstable, which results in a more bubbles around the core, causing the image processing code to overestimate the actual core size. The gas core velocities and averages found in this thesis align with those found in literature where they range from 1-10 $\mathrm{m\,s^{-1}}$ and the average is around from 3-7 $\mathrm{m\,s^{-1}}$ [14, 16, 25]. An important note to be added to these results is that the gas core void fraction has a large standard deviation around the calculated points. This is due to a number of reasons, first the flow is dynamic and the core size is often changing in size, this already causes the standard deviation to be larger. Second, the images that were used for the processing were not ideal for this, as they were the same images used for the flow identification where the sharpness of the interface was not the most important, this can then result in the code to misidentify the interface for example due to bubbles which are present. Therefore both the core void fraction and velocities are more of an indication rather than the true values.

5.2.2. Transition downstream of the swirl elements

From the previous section it became clear that the transition between the regular flow patterns and the swirling flow patterns downstream of the swirl were independent of u_{sg} and is therefore a horizontal line. The liquid superficial velocity of the transition is determined by a singular value, as shown in Figure 5.3. This procedure is also done for the maps of swirl elements 2 and 3, which are shown in appendix C. An important result was found when these transition points were analysed. A constant value is roughly obtained when the u_{sl} of the transitions are multiplied with the tangent of the swirl elements respective angles, this is shown in table 5.1.

Table 5.1: Tan(Θ) of the different swirl elements with the transition values of u_{sl}, multiplication of these results in a near constant value

Swirl element	**Tan(Θ)**	$\boldsymbol{u_{sl}}$	$\boldsymbol{u_{sl} \cdot \tan(\Theta)}$
1	0.845	0.30	0.25
2	1.26	0.20	0.25
3	1.97	0.13	0.26
4	3.27	0.08	0.26

This already gives a good indication that the transition from swirling to non-swirling flow patterns is connected to u_θ, as the Swirl number (Ω) is proportional to tan(Θ). This results agrees with two papers where a tangential cyclone was used to generate to swirling motion[15, 16]. In these papers two different swirl numbers were used where the transition u_{sl} multiplied with the swirl number resulted in a constant value. The product constant for their work too, though it is not the same value as obtained in this thesis.

In Chapter 3, two different equations for u_θ were found based on different assumptions on the conditions inside the swirl element as these were unknown. The equations obtained in the previous section can now be used to calculate the void fraction and gas core radius based on upstream conditions which are needed to calculate u_θ at the transition from non-columnar to columnar flows. This is done for two points of every swirl element, one with a low gas flow rate and one with a high gas flow rate, the results are shown in tables 5.2 and 5.3

Table 5.2: Values of $u\theta$ at the transition for all the swirl elements for a low gas flow rate calculated using equations 3.16 ($\boldsymbol{u_{\theta,1}}$) and 3.20 ($\boldsymbol{u_{\theta,2}}$). The pressure difference at the transition is also given for both ways of calculating $\boldsymbol{u_\theta}$

Swirl element	$\boldsymbol{u_{sl}}$ ($\mathrm{m\,s^{-1}}$)	$\boldsymbol{u_{sg}}$ ($\mathrm{m\,s^{-1}}$)	$\boldsymbol{u_{\theta,1}}$ ($\mathrm{m\,s^{-1}}$)	$\boldsymbol{u_{\theta,2}}$ ($\mathrm{m\,s^{-1}}$)	$\boldsymbol{\Delta p_1}$ (Pa)	$\boldsymbol{\Delta p_2}$ (Pa)
1	0.30	0.024	0.77	0.78	1053	1075
2	0.20	0.024	0.77	0.77	1049	1067
3	0.13	0.020	0.79	0.79	1109	1121
4	0.082	0.023	0.81	0.82	1147	1166

Table 5.2 confirms to suspicion that the transition from non-columnar flow to columnar flow types is dependent on u_θ as the values are roughly constant at 0.79 $\mathrm{m\,s^{-1}}$ for both equations of u_θ. This result should however be taken with a grain of salt as there are quite some assumptions involved. The patterns are determined via human observation, this can result in a slight deviation from the criteria set in chapter 4 for each swirl element. However, a small change in u_{sl} can result in a relatively large change in u_θ such that a shift of 0.01 $\mathrm{m\,s^{-1}}$ can result in a change of approximately 0.10 $\mathrm{m\,s^{-1}}$ for swirl element 4. Furthermore, as some

Table 5.3: Values of $u\theta$ at the transition for all the swirl elements for a high gas flow rate calculated using equations 3.16 ($\boldsymbol{u_{\theta,1}}$) and 3.20 ($\boldsymbol{u_{\theta,2}}$). The pressure difference at the transition is also given for both ways of calculating $\boldsymbol{u_\theta}$

Swirl element	$\boldsymbol{u_{sl}}$ (ms^{-1})	$\boldsymbol{u_{sg}}$ (ms^{-1})	$\boldsymbol{u_{\theta,1}}$ (ms^{-1})	$\boldsymbol{u_{\theta,2}}$ (ms^{-1})	$\boldsymbol{\Delta p_1}$ (Pa)	$\boldsymbol{\Delta p_2}$ (Pa)
1	0.30	0.50	0.67	0.98	235	504
2	0.20	0.50	0.74	0.85	435	577
3	0.13	0.50	0.79	0.85	532	614
4	0.083	0.52	0.88	0.91	611	655

big assumptions have been made on the conditions in the swirl element and in calculating the size of the core, this u_θ is more of an indication than the actual value. Further research should be done to determine the actual value of u_θ at the transition.

Table 5.3 shows a slightly different trend, for u_θ calculated according to equation 3.16 shows a larger dependence on the gas flow rate for the stronger swirl elements. Following from equation 3.16, this was expected as the gas flow rate has a higher influence for low liquid flow rates. As a result of this, u_θ decreases for swirl element 1, but increases for swirl element 4 in relation to the values with a low gas flow rate. When u_θ is calculated according to equation 3.20, it is more or less constant again, but is now larger which is expected. It should be noted that for both of these the intermittent characteristics of slug and churn flow has not been taking into account, which would further increase the liquid velocity in slugs, further research should be performed to identify this influence.

The importance of u_θ is due to its role in generating the pressure difference between the pipe wall and the gas core. As mentioned in chapter 3, the pressure difference is responsible for the formation of the core. The pressure difference can be approximated using equations 3.4 and 3.5 and the values of u_θ and α_g at the transitions. The pressure difference is roughly between 1000 Pa to 1200 Pa for the situation with a low gas flow and roughly between 200 Pa to 700 Pa for the situation with a higher gas flow. For a lower gas flow rate the pressure difference at the transition seems to be approximately constant which is inline with the model from chapter 3. For the situation with a higher u_{sg} the pressure differences decrease which suggest that the Δp is not a constant value for the transition. What is not considered in the model developed in this thesis, is that the liquid velocity will increase for larger u_{sg}, which increases u_θ, such that the Δp might be a constant at the transition. Just as with u_θ, these values should be taken with a grain of salt and are more of an indication than a precise value. Further research should be done in order to investigate if Δp is constant at the transition from non-columnar to columnar flow regimes. Another important note is that the average void fractions were used here to calculate R_g and Δp. In the slug and churn patterns, there is a large standard deviation in α_{core} due to the larger bubbles. It is possible that Δp is similar to the situation with a low gas flow rate, such that criteria set in chapter 3 still holds for the liquid slugs.

5.2.3. Transition close to the pick up tube

Plotting the line on the transition between regular and swirling flow patterns can also be done for the maps close to the pick up tube. As the decay is now dependent on u_{sg} the transition line is now not a horizontal line anymore, but consists of a increasing part which is roughly linear, after which the transition seems to be independent of u_{sg} again. Doing this yields the lines which can be seen in figure 5.5 and those in figures C.2b and C.3b, the transition values for u_{sl} are listed in table 5.4. These are values of u_{sl} at the left side of the figures, where u_{sg} is around $0.03\,\mathrm{ms}^{-1}$, which is similar to the values given in table 5.2.

Table 5.4: Transition values of u_{sl} close to the pick up tube with a low gas flow rate, u_θ is calculated by decaying the values of equations 3.16 ($u_{\theta,1}$) and 3.20 ($u_{\theta,2}$). The pressure differences of resulting from both u_θ are also shown

Swirl element	$\boldsymbol{u_{sl}}$ (ms^{-1})	$\boldsymbol{u_{sg}}$ (ms^{-1})	$\boldsymbol{u_{\theta,1}}$ (ms^{-1})	$\boldsymbol{u_{\theta,2}}$ (ms^{-1})	$\boldsymbol{\Delta p_1}$ (Pa)	$\boldsymbol{\Delta p_2}$ (Pa)
1	0.45	0.035	0.61	0.62	670	684
2	0.33	0.023	0.66	0.67	806	812
3	0.20	0.019	0.64	0.64	750	763
4	0.14	0.024	0.76	0.76	1051	1055

To calculate the tangential velocity close to the pick up tube equations 3.16 and 3.20 can be used again. However, u_θ decays along the length of the pipe. This decay is synonymous to that of the swirl number given in equation 2.21. By using this equation and a length of 1.3 m, u_θ at the pick up tube can be approximated.

Surprisingly, the values of u_θ close to the pick up tube are lower than those in table 5.2 while they now also span a slightly larger range of around $0.15\,\mathrm{m\,s^{-1}}$ for both ways of calculating the tangential velocity. This might be due to a number of reasons. The decay factor used to calculate the decayed values is 0.04, this was taken from Dirkzwager which was for single phase flow. For multiphase flow, the decay factor might be different as this depends several factors such as the Reynolds number, the swirl number wall roughness and inlet conditions[6]. For an increasing Reynolds number, the decay factor decreases, a possible reason for this is that the friction factor decreases for increasing Reynolds numbers[6, 29]. Furthermore, for a higher swirl number the decay factor will also be larger. Both of these indicate that the decay factor should be different for the different swirl elements, this might then result in the values of u_θ being closer to those found in table 5.2. Another possible explanation for the lower values might be that the formation of the core requires a larger u_θ than it needs for existing such that the core remains even though u_θ is lower. As the actual u_θ close to the pick up tube is not known, further research should be done in order to determine this. In contrast to the previous section, the transition values for u_{sl} are now dependent on the gas velocity. In table 5.5 the transition values are shown for a gas flow rate where the transitions became constant again.

Table 5.5: Transition values of u_{sl} close to the pick up tube with a high gas flow rate, u_θ is calculated by decaying the values of equations 3.16 ($u_{\theta,1}$) and 3.20 ($u_{\theta,2}$). The pressure differences of resulting from both u_θ are also shown

Swirl element	$\boldsymbol{u_{sl}}$ ($\mathrm{m\,s^{-1}}$)	$\boldsymbol{u_{sg}}$ ($\mathrm{m\,s^{-1}}$)	$\boldsymbol{u_{\theta,1}}$ ($\mathrm{m\,s^{-1}}$)	$\boldsymbol{u_{\theta,2}}$ ($\mathrm{m\,s^{-1}}$)	$\boldsymbol{\Delta p_1}$ (Pa)	$\boldsymbol{\Delta p_2}$ (Pa)
1	0.56	0.45	0.66	0.82	333	511
2	0.43	0.46	0.83	0.92	720	873
3	0.32	0.43	0.98	1.05	1081	1230
4	0.24	0.44	1.23	1.32	1597	2054

An interesting observation can be made when comparing the transition values with a higher u_{sg} to those with a lower u_{sg}. Where the values of u_θ with a low u_{sg} were all still relatively close to each other, those obtained with a larger u_{sg} display a larger spread of around $0.5\,\mathrm{m\,s^{-1}}$ for both ways of calculating u_θ. This seems to suggest that u_{sg} influences the decay much more for higher swirl intensities then lower swirl intensities. The differences between these tables 5.4 and 5.5 also clearly show that u_{sg} has a big influence on the decay as the values of u_{sl} increase with quite a margin. The u_{sl} of the transition is now higher than the u_{sl} with a low gas flow rate, as the gas influences the decay of the swirl.

When the pressure difference is calculated with the decayed values of u_θ for the situation with a low gas flow rate, it ranges from 700 to 1100 Pa depending on the swirl element. This is generally lower than the Δp found in section 5.2.2 for the similar void fraction. This might be due to the same reasons which were previously discussed, it can be that the core needs a smaller Δp to keep existing than it needs to form or that the wrong value for C_{decay} is used. It is also possible that the pick up tube influences the formation of the core, which might cause the core to form at a lower Δp.

When the Δp is calculated for the situation with a high gas flow rate, it is found to be between 300 to 1600 Pa when $u\theta$ is found using equation 3.16 and between 500 to 2000 Pa when equation 3.20 is used. This is a much larger range than for the situation with a low gas flow rate. If a constant Δp dictates the transition from non-columnar to columnar flow it might be that the gas flow rate influences the decay factor. A large range of Δp is then obtained, if only one value for C_{decay} is used, as the decay is then wrongly calculated. All of the pressure differences are more of an indication however, as these were calculated by using u_θ, for which some large assumptions have been made. Further research should be performed in order to accurately determine Δp and investigate if it is a constant value or not, it can then also be investigated whether there is a difference between the positions close to the swirl element and close to the pick up tube.

5.3. Transitions in the swirling region

After closely observing the flow pattern maps, it seemed that the transition between swirling column and swirling pulsating and the transition between swirling column and swirling burst seem to follow the transition criteria defined by Taitel et al. [19]. The pattern swirling pulsating seems to originate from non-homogeneous bubbly flow, while the burst is connected to the transition from bubbly to slug or churn flows. To see if this was actually the case, the transition line based on equation 2.7 is plotted in the maps for swirl element 2 and 4.

In Figures 5.8a and 5.8b, two lines are plotted both based on equation 2.7, but using different void frac-

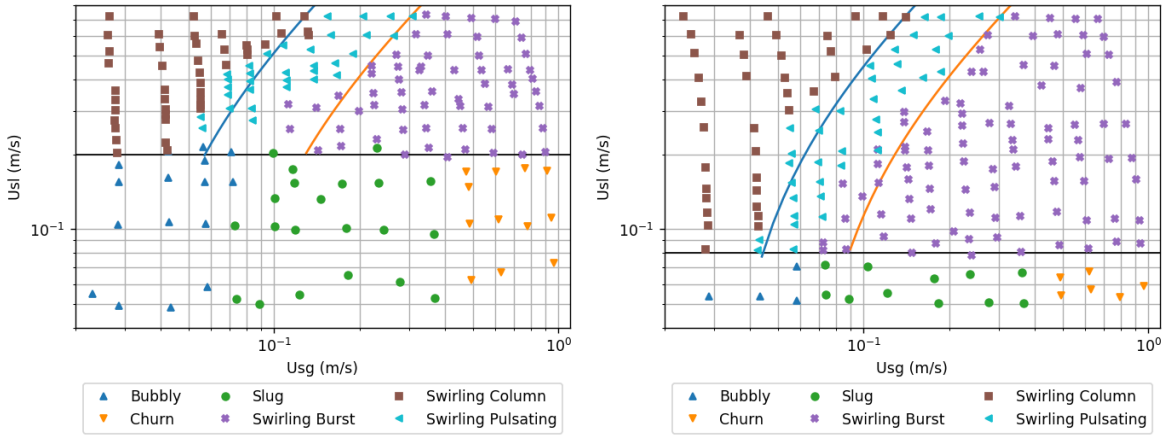

Figure 5.8: The flow pattern maps of swirl element 2 and 4 with the transition lines based on equation 2.7, The blue line considers and α_g of 0.12 for swirl element 2 and 0.13 for swirl element 4, while the orange line considers an α_g of 0.25

tions. The orange line is with the standard void fraction of 0.25 which lines up nicely between the transition of swirling pulsating to swirling burst. A potential reason for this was previously mentioned as the patterns slug and churn have alternating flow rates, this then causes the patterns downstream to be more unstable causing a less stable flow Because swirling burst is defined as a more unstable version of swirling pulsating, this will then be present when the upstream conditions are more chaotic. The chaotic nature of swirling burst is then also a possible reason that this transition happens sooner for swirl element 1, as this is too weak to contain the pulses generated by either slug or churn flow. For swirl element 1, the transition happens at an α_g of approximately 0.1. The maps of swirl elements 1 and 3 with the additional transition lines are show in appendix C. The left line is plotted using a different void fraction, that was slightly different for every swirl element used, it ranged from a void fraction of around $0.10 - 0.13$. This range can be explained due to the definitions of the flow patterns. There are always some pulsations present in the flow patterns, even in the swirling column which is the most stable. The pulsations originate from larger bubbles upstream and are compresses inside the columnar flow, a higher swirl intensity may cause dampening of the pulsations causing similar flow rates to cause different patterns when comparing swirl elements. Following this, a small investigation was done on when these larger bubbles start forming and one can start expecting the pulsating columns to form. From this it was found that the larger bubbles start forming at a void fraction calculated using equation 2.2 of around 0.1. This can be seen in Figure 5.9 for different combinations of u_{sg} and u_{sl}.

5.4. Comparing the proposed model with data from literature

The start of a mechanistic model was constructed in chapter 3. To verify this, data found in literature can be used. Comparing the model to the data from Liu and Bai [8] will be difficult, as from their papers it appears that the condition to call a pattern swirling intermittent, which is analogous to the patterns swirling pulsating and swirling burst of this thesis, is much less strict than in this thesis. For this reason their data will not be used to calculate the pressure difference at the transition from columnar to non columnar flow types. Shakutsui et al. [15] used a tangential cyclone in their paper, from this paper it appears that they have similar definitions for the formation of columnar flow patterns. In order to calculate the pressure difference between the wall and the interface for their setup, the tangential velocity profile needs to be known. From literature it appears that the tangential cyclones follow a similar profile to those used in this thesis with an inner forced vortex region and an outer roughly constant velocity[30–32]. There is some difference however as the critical core radius (R_c) appears to be around $0.4R$ instead of $0.25R$. Using this information and equations 3.4 and 3.5, the pressure difference for the transition from Shakutsui et al. can be found. The setup of Shakutsui et al. makes use of a pipe with an ID of 30 mm and their visualisation is done 600 mm from the exit of the tangential cyclone. A more detailed description of their setup up and on how their u_θ and Δp are calculated can be found in appendix E. With this information, the pressure difference can be approximated to be around 1.07×10^4 Pa for low flow rates of gas when a core void fraction of 0.027 is used and roughly 8.9×10^3 Pa for higher flow rates of gas, when a core void fraction of 0.10 is used. A core void fraction of 0.10 is used, as the results shown

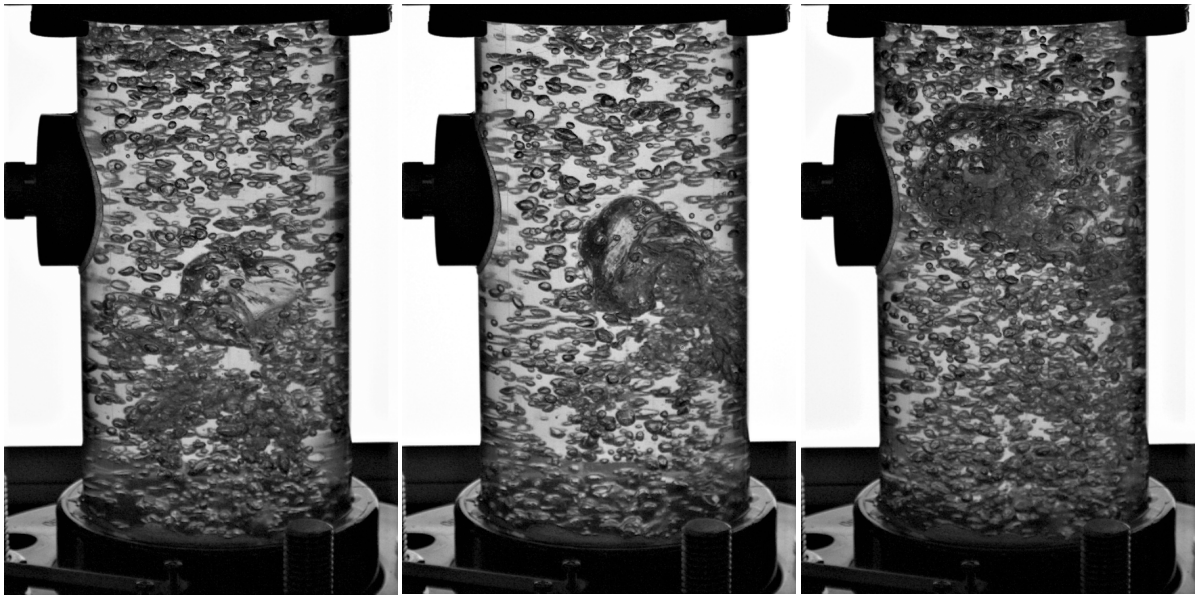

(a) u_{sl} 0.23 ms^{-1}, u_{sg} 0.022 ms^{-1} (b) u_{sl} 0.29 ms^{-1}, u_{sg} 0.027 ms^{-1} (c) u_{sl} 0.54 ms^{-1}, u_{sg} 0.051 ms^{-1}

Figure 5.9: Bigger bubbles upstream for different flow rates with an α_g of around 0.10, swirl element 3 is used in all the images.

in table 5.3 also have a core void fraction of roughly 0.10. These pressure differences are much larger than those calculated in this thesis, which can have a couple of explanations. One is that the equations used to calculate u_θ in this thesis are an underestimation, this is not likely however, as for low gas flow rates, the axial liquid velocity will be very similar to u_{sl}. As u_θ is coupled to $u_{z,se}$, a good prediction of u_θ can be assumed for low flow rates of gas. This indicates that the equations used most likely do not underestimate the tangential velocity. Another possible explanation is that there is some dependency on the pipe diameter. The ratio of cross-sectional areas (A_{thesis}/A_{paper}) is 7.4, while the ratio of pressure differences ($\Delta p_{paper}/\Delta p_{thesis}$) found is roughly 8.1, from this it seems that the pressure difference inversely scales with the cross-sectional area. As there is almost no further data available on this, it should be investigated in further research.

6

Conclusion and Recommendations

The first goal of this thesis was to investigate for the first time the effect of different strengths of swirl element on the swirling gas-liquid flow regime maps. Four swirl elements with the same geometry but varying vane angles were used to investigate this, these swirl elements were labelled 1-4 where swirl element 1 has the lowest vane angle and 4 has the highest vane angle. The experiments were performed within a range of $0.03\,\mathrm{m\,s^{-1}}$ to $0.70\,\mathrm{m\,s^{-1}}$ for u_{sl} and within $0.02\,\mathrm{m\,s^{-1}}$ to $1.00\,\mathrm{m\,s^{-1}}$ for u_{sg}. The first important result found in this thesis is that the transition from non-columnar flows to columnar flows close to the swirl element is independent of the gas flow rate at least for the range used in this thesis. This coincides with what can be found in literature. The second important result found in this thesis is that the transition from non-columnar flows to columnar flows is highly dependent on the strength of the swirl element which is used. The transition from non-columnar to columnar flows happened at a superficial liquid velocity of $0.30\,\mathrm{m\,s^{-1}}$ for swirl element 1 while it happened at an u_{sl} of $0.08\,\mathrm{m\,s^{-1}}$ for swirl element 4 with the other two swirl elements in between these. u_{sl} when the transition takes place changes for each swirl element, its product with the vane angle is constant for the setup. Within the columnar region, three different flow types where identified: swirling column, swirling pulsating and swirling burst. Swirling column is a highly stable gas column with almost no pulsations in the column. Swirling pulsating is a stable gas column which presents pulsations connected to the passage of larger bubbles through the swirl element. The upstream conditions are still bubbly, such that the pulsations are not sufficient to break the gas column in to a burst of small bubbles. This does happen for the pattern swirling burst, where the passage of large bubbles causes the core to break into small bubbles.

Flow pattern maps close to the pick up tube were also created to investigate the effect of decay on the flow regime maps. This was done at a z/D of roughly 16. In contrast to the flow regime maps close to the swirl element, the transition from non columnar flow types to columnar flow types is now dependent on the gas flow rate. For a higher gas flow rate, a higher liquid flow rate is needed as well in order to achieve columnar flow types. From these maps it could also be observed that the transition now takes place at a higher u_{sl} when compared to the maps close to the swirl element, which is expected due to the decay of the swirl along the pipe length. For the maps close to the pick up tube a new flow pattern was defined, which is swirl dying. This pattern still somewhat resembles a columnar flow type though the column now has fallen apart into large bubbles.

The second goal of this thesis was to try and construct a mechanistic model to predict the transition between the non-columnar flows and columnar flow types. A mechanistic model was proposed in this thesis, the model suggests that the transition from non-columnar to columnar flow happens at a certain Δp, meaning that the driving force for the transition is constant. The model also suggests that the flow regimes upstream, determine the patterns downstream such that for example slug flow results in the pattern swirling burst downstream.

The results found in this thesis showed that the model seems to be correct for a situation with a low gas flow rate. The transition from non-columnar to columnar flow rates happens at a Δp of roughly 1000 Pa to 1200 Pa for low flow rates of gas, indicating that the driving force for the separation is roughly constant. For larger flow rates of gas this pressure difference was mostly lower due to the larger core size, but similar u_θ, with a range between 200 Pa to 700 Pa. This could indicate that the driving force might not be constant over the whole range. When the Δp is calculated for the points close to the pick up tube, it is around 700 Pa to 1100 Pa for low flow rates of gas. It is slightly lower, meaning that the driving force to maintain the gas column might be slightly smaller than the driving force to form the gas column. For higher flow rates of gas the pressure difference ranged between 300 Pa to 2000 Pa, which suggests that the model might not be correct as

the driving force now spans a large range. These results should be taken with a grain of salt, as both u_θ and Δp are more of an indication due to all of the assumptions made. The prediction that the upstream conditions determine the downstream conditions appears to be true, when the transition line from bubbly to slug flow is plotted inside the flow regime maps it coincides with the transition from swirling pulsating to swirling burst. The transition from swirling column to swirling burst follows the trend but for a lower void fraction.

The beginning of a mechanistic model was developed in this thesis. However, it has a large number of unknowns and is based on assumptions which do not have a strong base. The most important parameters for this model contained large uncertainties, such that drawing a strong conclusion on the transition criteria for non-columnar flow and columnar flow is not possible. The same uncertainties hold for the decay of u_θ, where there is an extra unknown within the decay factor. Only a singular value was used, while in reality this depends on a number of parameters, such that it will be different for each swirl element and the various flow conditions used. The pressure differences for the transition from non-columnar to columnar flow from this thesis, were not consistent with those found in literature. For a smaller pipe diameter, the pressure difference seems to increase. It was calculated that the pressure difference at the transition from non-columnar to columnar flow types, ranged from 8.9×10^3 Pa to 1.07×10^4 Pa for a pipe diameter of 30 mm. The ratios of cross-sectional areas and pressure differences were calculated. This suggested that there is a relation between the pressure difference and the cross-sectional area at the transition from non-columnar to columnar flow types. From this it seems that the driving force that is needed to form the column, is connected in some way to the cross-sectional area. Based on the uncertainties involved in the parameter used to estimate the transition and the mismatch with the literature for a smaller pipe diameter, it is suggested to:

- **Investigate the effect of the pick up tube and flow straightener** : In this thesis a set up with a pick up tube and a flow straightener was used while in literature available this was not present. The flow straightener recovers the static pressure, while the pick up tube enables separation. It should be investigated whether this has an influence on the formation of the columnar flow patterns or not.

- **Investigate the effect of the air sparger**: The air sparger can change the incoming conditions such that larger or smaller bubbles are present in the flow. This can then effect the flow types after the swirl element as the depend heavily on the incoming conditions

- **Investigate the effect of pipe diameter**: Only one pipe diameter was used in this thesis. The effect of pipe size for similar swirl geometry should be investigated as this could influence the formation of the columnar flow types as well as change the incoming conditions. From literature it was found that the transition to columnar flow patterns was not dependent on a singular value of Δp, it rather seems to be a combination between pressure difference and pipe diameter.

- **Measure the pressure at the wall and within the core**: In order to investigate what drives the formation of the core, the pressure at the wall and within the core should be analysed to determine if the transition from non-columnar to columnar flow is due to a constant pressure difference or if some other effect determines the transition.

- **Investigate the conditions in the swirl element**: The swirl element used in this thesis was not transparent, therefore it could not be seen what happened within the swirl element. A transparent swirl element should be used in order to see what is happening in the swirl element to verify if the assumption on flow separation is correct or not when estimating u_θ.

- **Propose a quantitative criteria to categorise the columnar flow patterns**: To help differentiate the columnar flow patterns, probability density functions can be constructed to help identify the patterns as now they are determined by human observation which can cause bigger errors in identification

- **Investigate the influence of flow split**: Both valves after the pick up tube were open during the experiments in this thesis. Changing the valves changes the flow split, quick testing showed that this influences the whole core size and formation of columns close to the pick up tube. Closing the inner tube valve will for example result in a larger core, further research should be done to investigate this effect.

Bibliography

[1] Laurens Joseph Arnold Marie Van Campen. *Bulk dynamics of droplets in liquid-liquid axial cyclones*. PhD thesis, Technische Universiteit Delft, 2014.

[2] Sabrina Kelbij Star. Pressure distribution in a liquid-liquid separator. Master thesis, Technische Universiteit Delft, April 2016.

[3] John Michael Walsh, Wally John Georgie, et al. Produced water treating systems-comparison between north sea and deepwater gulf of mexico. In *SPE Annual Technical Conference and Exhibition*. Society of Petroleum Engineers, 2012.

[4] Benjamin Sahovic, Hanane Atmani, Muhammad Awais Sattar, Matheus Martinez Garcia, Eckhart Schleicher, Dominique Legendre, Eric Climent, Remi Zamansky, Annaig Pedrono, Laurent Babout, et al. Controlled inline fluid separation based on smart process tomography sensors. *Chemie Ingenieur Technik*, 92(5):554–563, 2020.

[5] Olav Kristiansen. Compact, inline separation technology-what and why? Website `https://www.yumpu.com/en/document/read/23496728/compact-inline-separation-technology-a-what-and-why-ntnu`, 2013.

[6] Maarten Dirkzwager. *A new axial cyclone design for fluid-fluid separation*. PhD thesis, Technische Universiteit Delft, december 1996.

[7] Jaseer E Hamza, Hussain H Al-Kayiem, and Tamiru A Lemma. Experimental investigation of the separation performance of oil/water mixture by compact conical axial hydrocyclone. *Thermal Science and Engineering Progress*, 17:100358, 2020.

[8] Li Liu and Bofeng Bai. Flow regime identification of swirling gas-liquid flow with image processing technique and neural networks. *Chemical Engineering Science*, 199:588–601, 2019.

[9] Hussain H Al-Kayiem, Jaseer E Hamza, and Tamiru A Lemmu. Performance enhancement of axial concurrent liquid–liquid hydrocyclone separator through optimization of the swirler vane angle. *Journal of Petroleum Exploration and Production Technology*, 10(7):2957–2967, 2020.

[10] Geoffrey Frederick Hewitt and DN Roberts. Studies of two-phase flow patterns by simultaneous x-ray and flast photography. Technical report, Atomic Energy Research Establishment, Harwell, England (United Kingdom), 1969.

[11] George Yadigaroglu and Geoffrey F Hewitt. *Introduction to multiphase flow: basic concepts, applications and modelling*. Springer, 2017.

[12] Benjamin Wu, Mahshid Firouzi, Travis Mitchell, Thomas E Rufford, Christopher Leonardi, and Brian Towler. A critical review of flow maps for gas-liquid flows in vertical pipes and annuli. *Chemical Engineering Journal*, 326:350–377, 2017.

[13] KW McQuillan and PB Whalley. Flow patterns in vertical two-phase flow. *International Journal of Multiphase Flow*, 11(2):161–175, 1985.

[14] Li Liu, Ke Wang, and Bofeng Bai. Experimental study on flow patterns and transition criteria for vertical swirling gas-liquid flow. *International Journal of Multiphase Flow*, 122:103113, 2020.

[15] Hideaki Shakutsui, Katsutoshi Watanabe, Hirofumi Onari, Takanori Saga, and Hiroshi Kadowaki. Flow patterns in swirl gas-liquid two-phase flow in a vertical pipe. In *Proceedings of the 4th JSME-KSME Thermal Engineering Conference*, volume 3, 2000.

[16] Hideaki Shakutsui, Kosuke Hayashi, and Takayuki Suzuki. Flow patterns of gas-liquid two-phase swirling flow in a vertical pipe. *Japanese Journal of Multiphase Flow*, 24(3):305–312, 2010.

[17] Wen Liu and Bofeng Bai. Swirl decay in the gas–liquid two-phase swirling flow inside a circular straight pipe. *Experimental Thermal and Fluid Science*, 68:187–195, 2015.

[18] Clayton T Crowe. *Multiphase flow handbook*, volume 59. CRC press, 2005.

[19] Yehuda Taitel, Dvora Bornea, and AE Dukler. Modelling flow pattern transitions for steady upward gas-liquid flow in vertical tubes. *AIChE Journal*, 26(3):345–354, 1980.

[20] Tibor Z Harmathy. Velocity of large drops and bubbles in media of infinite or restricted extent. *AIChE Journal*, 6(2):281–288, 1960.

[21] Osami Kitoh. Experimental study of turbulent swirling flow in a straight pipe. *Journal of Fluid Mechanics*, 225:445–479, 1991.

[22] Alireza Karimpoorheidari. A numerical study of swirl flow in pipes. Master thesis, Technische Universiteit Delft, December 2019.

[23] Jesse Jonathan Slot. *Development of a centrifugal in-line separator for oil-water flows*. PhD thesis, University of Twente, May 2013.

[24] Matheus Martinez Garcia. *Gas-Liquid Inline Separator (Tomocon)*. Technische Universiteit Delft, 2021.

[25] Muhammad Awais Sattar, Matheus Martinez Garcia, Robert Banasiak, Luis M Portela, and Laurent Babout. Electrical resistance tomography for control applications: Quantitative study of the gas-liquid distribution inside a cyclone. *Sensors*, 20(21):6069, 2020.

[26] Engineering Toolbox. Refractive index for some common liquids, solids and gases. Website `https://www.engineeringtoolbox.com/refractive-index-d_1264.html`, 2008.

[27] Crow. Refractive index of amorphous polymers. Website `http://polymerdatabase.com/polymer%20physics/Ref%20Index%20Table2%20.html`, 2021.

[28] John Taylor. *Introduction to error analysis, the study of uncertainties in physical measurements*. University Science Books, 1997.

[29] W Steenbergen and J Voskamp. The rate of decay of swirl in turbulent pipe flow. *Flow measurement and instrumentation*, 9(2):67–78, 1998.

[30] Mehdi Azadi, Mohsen Azadi, and Ali Mohebbi. A cfd study of the effect of cyclone size on its performance parameters. *Journal of hazardous materials*, 182(1-3):835–841, 2010.

[31] Khairy Elsayed and Chris Lacor. The effect of cyclone inlet dimensions on the flow pattern and performance. *Applied mathematical modelling*, 35(4):1952–1968, 2011.

[32] Omid Reza Nassaj, Davood Toghraie, and Masoud Afrand. Effects of multi inlet guide channels on the performance of a cyclone separator. *Powder Technology*, 356:353–372, 2019.

A

Derivation of the swirl number

The definition of the swirl number is the flux of angular momentum made dimensionless by using the the bulk velocity and pipe radius. The angular momentum generated in the swirl element is given by

$$\dot{L}_{se} = \dot{m} u_\theta (0.9 R_{se}) \tag{A.1}$$

Where $\dot{L}_{se}$ is the total angular momentum flux, $\dot{m}$ is the total mass flow, u_θ is the tangential velocity and $(0.9R_{se})$ is the average position in the swirl element. The total mass flow can be approximated by the liquid mass flow as $\rho_l \gg \rho_g$. The tangential velocity can be replaced by $u_{z,l,se}\tan(\Theta)$, such that the equation becomes

$$\dot{L}_{se} = \dot{m}_l u_{z,l,se} \tan(\Theta)(0.9 R_{se}) \tag{A.2}$$

The swirl number is made dimensionless using the velocity of the bulk and the pipe radius, as the mass of air is negligible only the mass of water is used, such that the equation for the swirl number becomes

$$\Omega = \frac{\dot{m}_l u_{z,l,se}(0.9 R_{se})}{\dot{m}_l u_{z,l,pipe} R} \tag{A.3}$$

The ratio of the velocity in the swirl element and the pipe follows from a conservation of mass

$$u_{z,pipe} A_{pipe} = u_{z,se} A_{se} \tag{A.4}$$

$$u_{z,pipe} \pi R_{pipe}^2 = u_z, se\pi (R_{se}^2 - R_b^2) \tag{A.5}$$

$$u_{z,se} = u_{z,pipe} \frac{R_{pipe}^2}{R_{se}^2 - R_b^2} \tag{A.6}$$

Where A_{pipe} is the area of the pipe, $A_s e$ is the area inside the swirl element, R_{se} is the radius of the swirl element and R_b is the radius of the vane body. The pipe radius is 40.7 mm, the swirl element radius is 50 mm and the vane body radius is 40 mm. With this the ratio of velocities can be found to be

$$u_{z,se} = 1.84 u_{z,pipe} \tag{A.7}$$

With this known the equation for the swirl number becomes

$$\Omega = \frac{1.657 \dot{m}_l u_{z,pipe} R_{se}}{\dot{m} u_{z,pipe} R} = 2.035 \tan(\Theta) \tag{A.8}$$

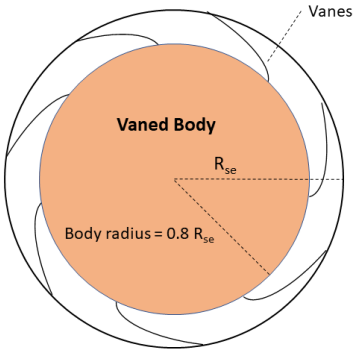

Figure A.1: Cross-section of the the swirl element, as also shown in chapter 2. Important to note is the inner body is $0.8R_{se}$

B

Dynamic behaviour of the columnar flow patterns

In this appendix, a sequence of images is shown for each flow type defined in chapter 2.2.4. The sequences better show the dynamic behaviour of each flow pattern, as this can be hard to see from just one image.

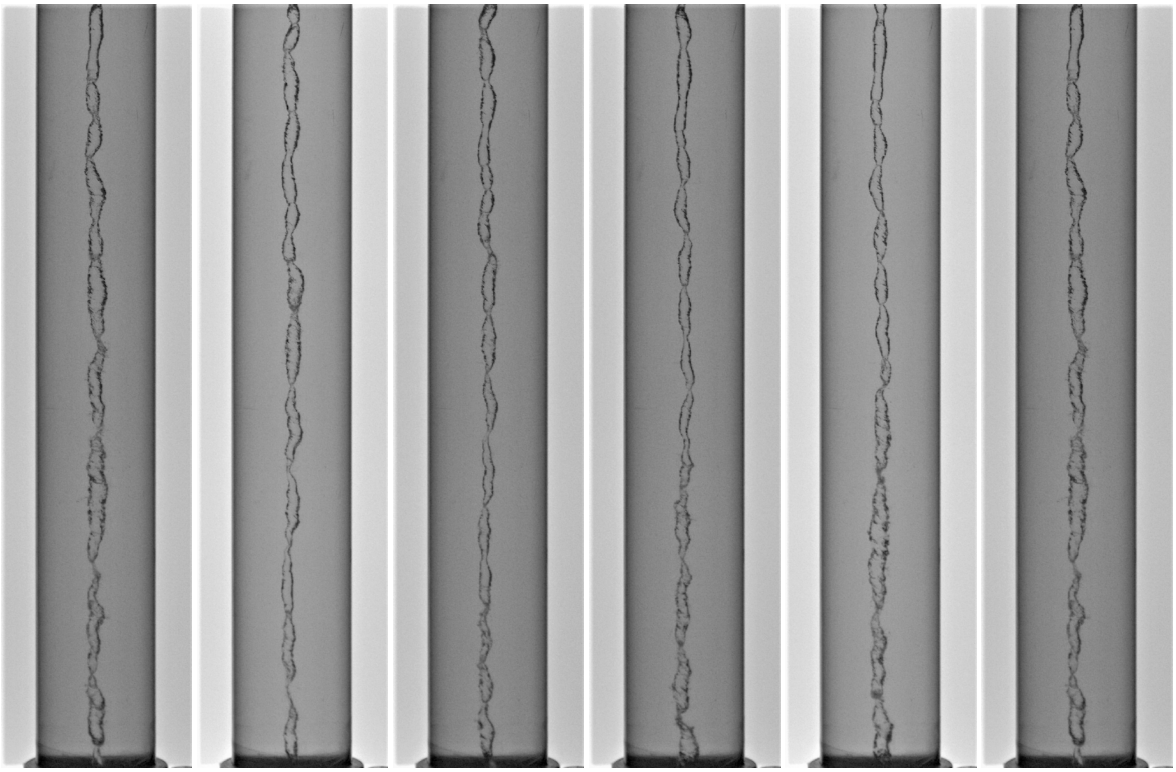

(a) (b) (c) (d) (e) (f)

Figure B.1: Dynamic behaviour of the swirling gas column pattern, taken for swirl element 4 at the following conditions $u_{sl} = 0.30\,\mathrm{m\,s^{-1}}$, $u_{sg} = 0.054\,\mathrm{m\,s^{-1}}$. It is clear that the patterns does not present any significant fluctuations in the interface.

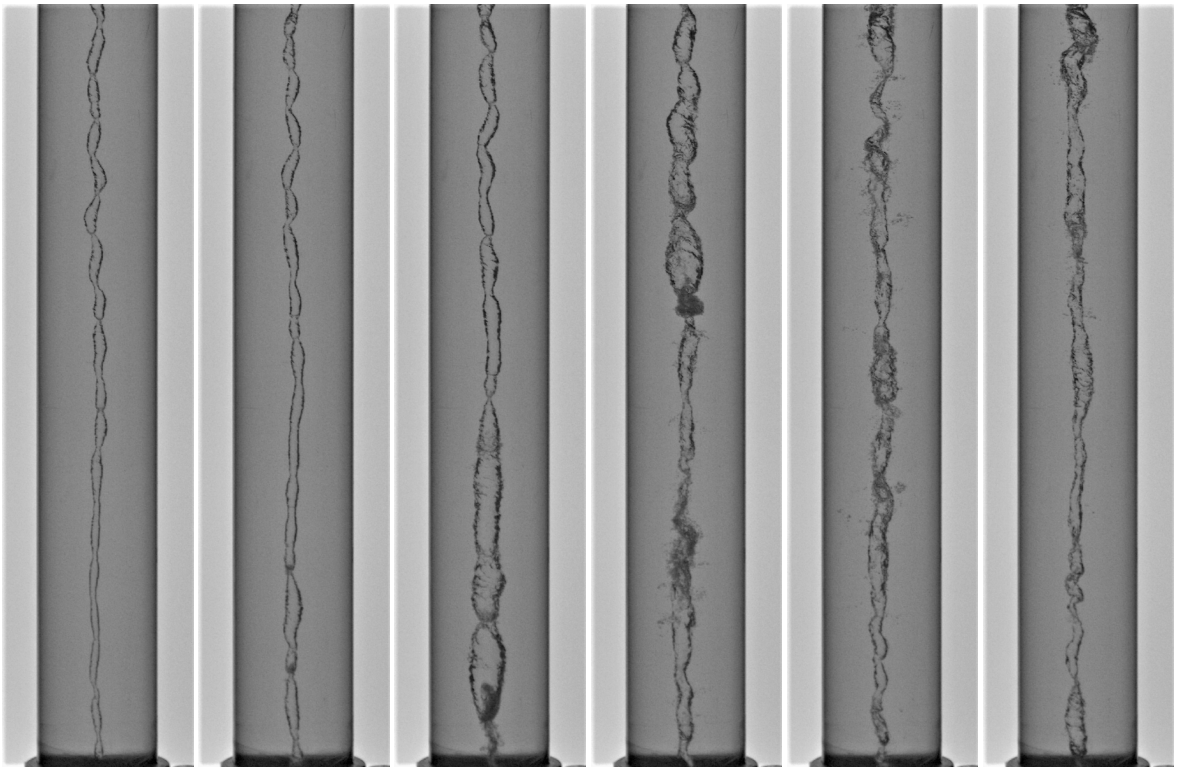

(a) (b) (c) (d) (e) (f)

Figure B.2: Dynamic behaviour of the swirling pulsating pattern, taken for swirl element 4 at the following conditions $u_{sl} = 0.25\,\mathrm{m\,s^{-1}}$, $u_{sg} = 0.069\,\mathrm{m\,s^{-1}}$. The passage of the pulse of gas is notable in figures c and d, while figures a and b represent the stable core present between the pulses.

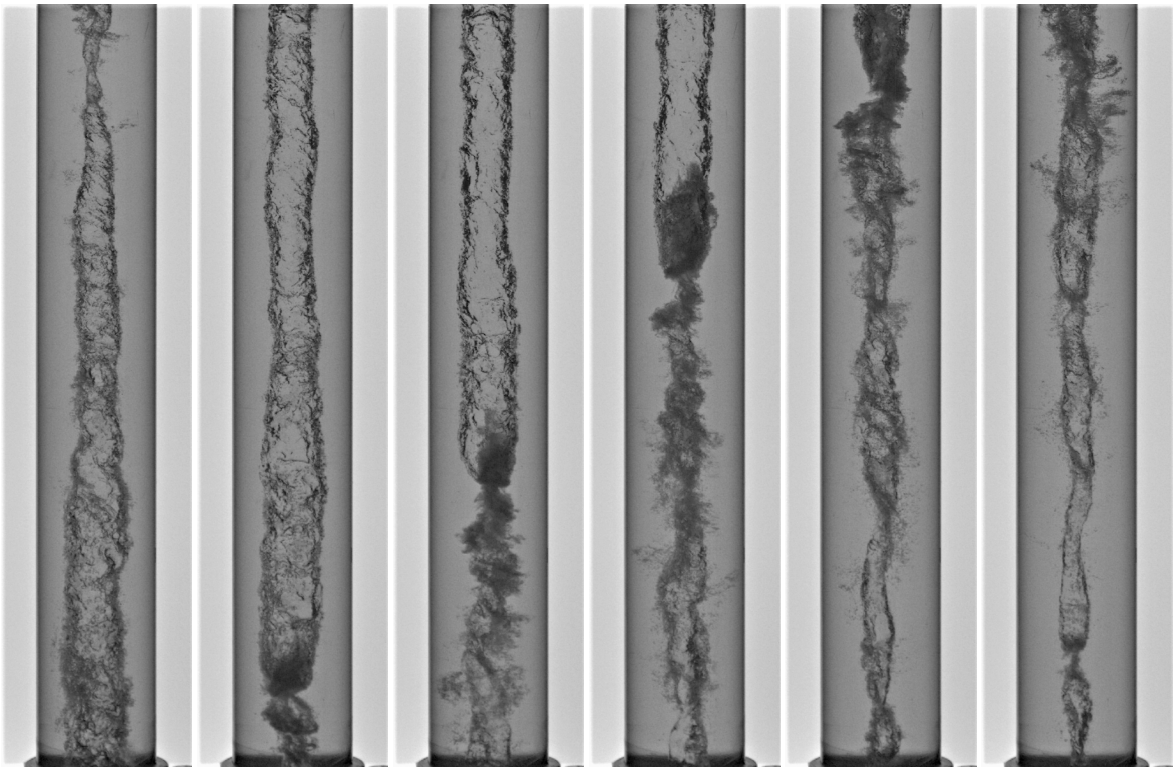

(a) (b) (c) (d) (e) (f)

Figure B.3: Dynamic behaviour of the swirling burst pattern, taken for swirl element 4 at the following conditions $u_{sl} = 0.60\,\mathrm{m\,s^{-1}}$, $u_{sg} = 0.27\,\mathrm{m\,s^{-1}}$. From the figures it is clear that the core breaks into a burst of bubbles after a sudden contraction.

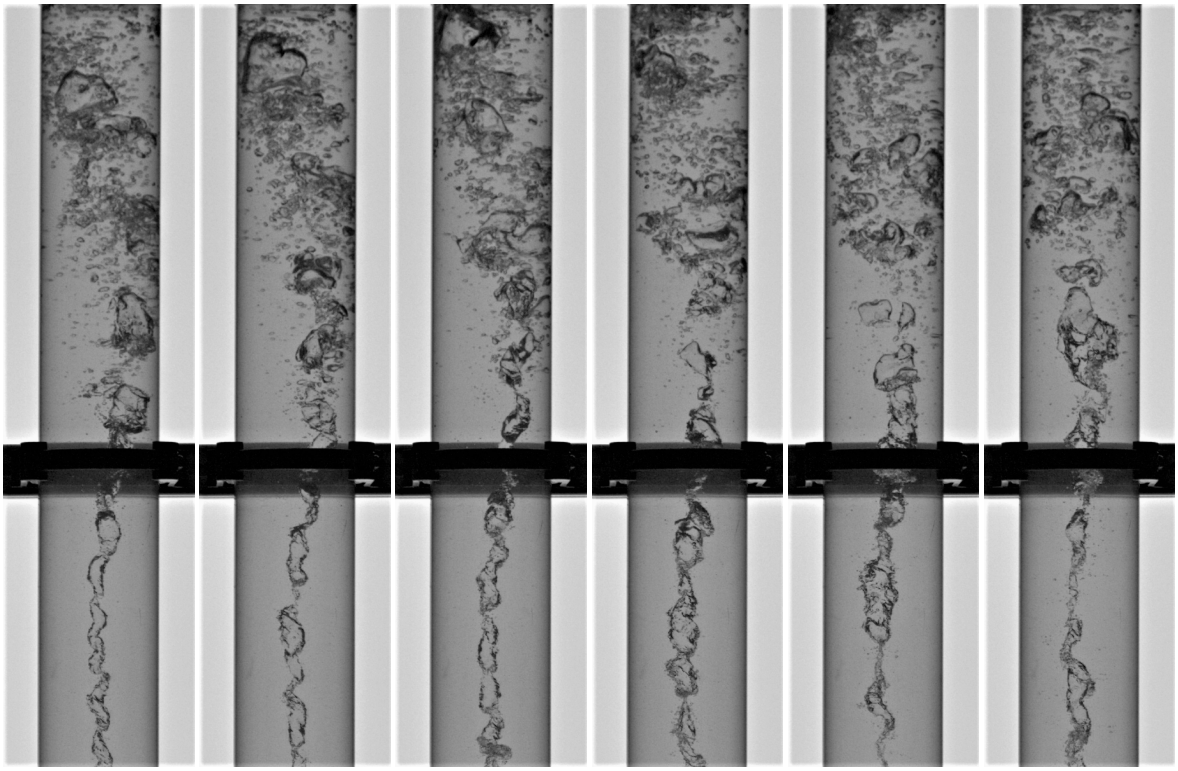

(a) (b) (c) (d) (e) (f)

Figure B.4: Dynamic behaviour of the swirl dying pattern, taken for swirl element 4 at the following conditions $u_{sl} = 0.13\,\mathrm{m\,s^{-1}}$, $u_{sg} = 0.028\,\mathrm{m\,s^{-1}}$. It is clear from the figures that the core present in the middle of the pipe loses axisymmetry and breaks into bubbles near the pick up tube.

C

Flow pattern maps

In this appendix all the flow regime maps from the swirling section are shown. These are the maps close to the swirl element and close to the pick up tube. Finally the map of swirl elements 1 and 3 are shown with the transition lines from Taitel et al.[19] plotted to indicate the transitions in the columnar region.

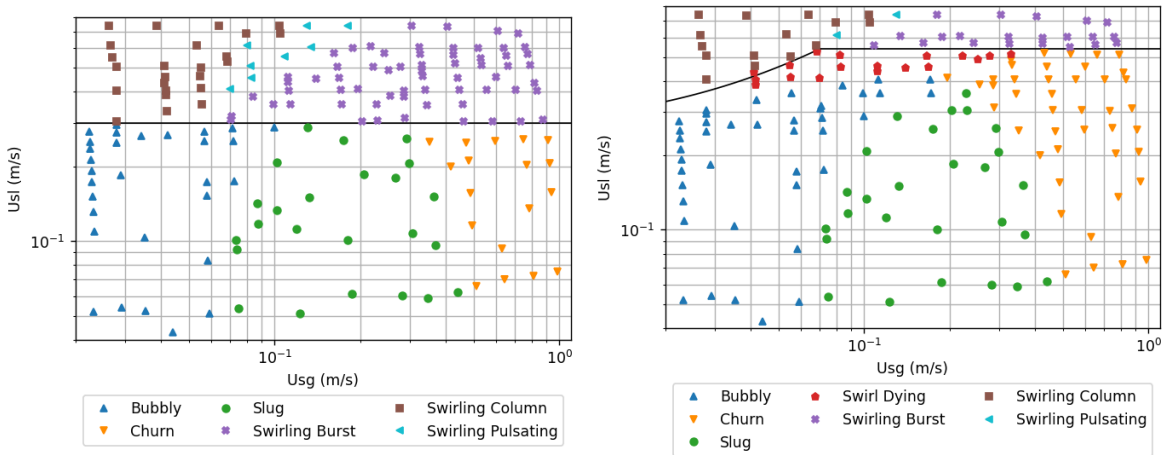

(a) (b)

Figure C.1: The flow pattern maps of swirl element 1 downstream of the swirl element and close to the pick up tube

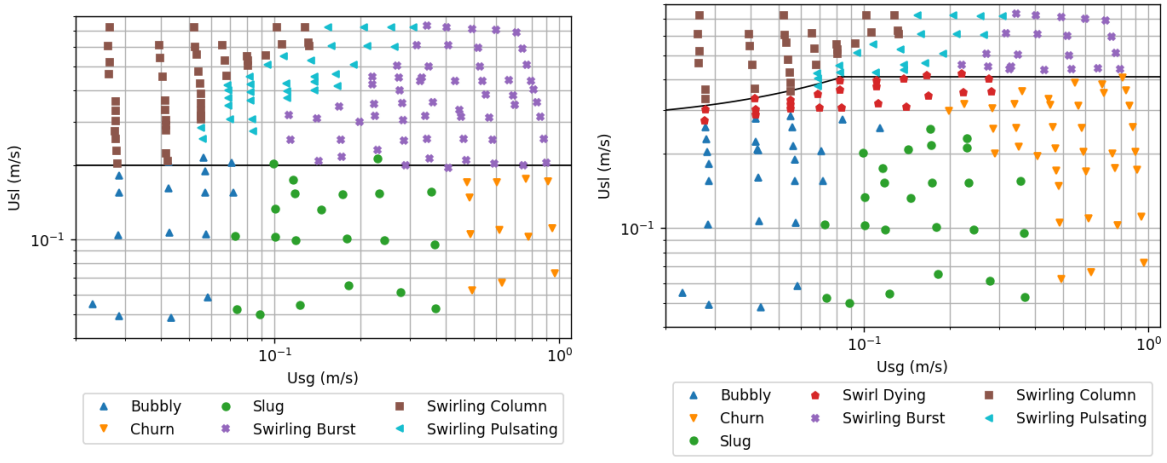

(a) (b)

Figure C.2: The flow pattern maps of swirl element 2 downstream of the swirl element and close to the pick up tube

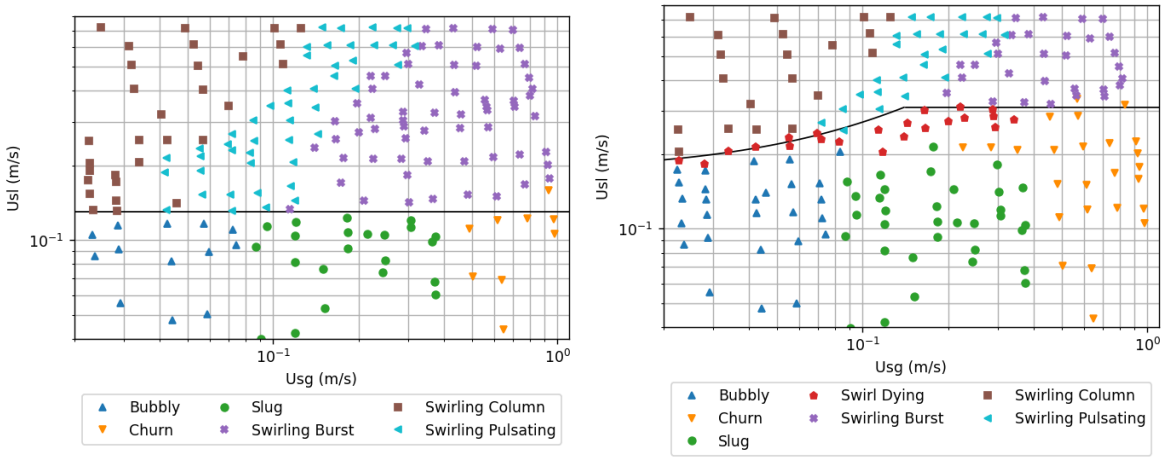

(a) (b)

Figure C.3: The flow pattern maps of swirl element 3 downstream of the swirl element and close to the pick up tube

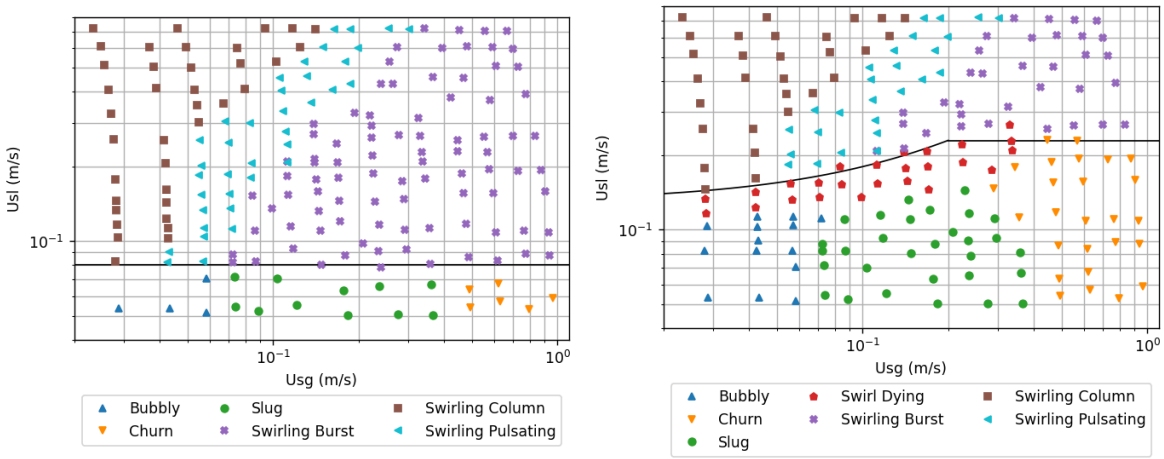

(a) (b)

Figure C.4: The flow pattern maps of swirl element 4 downstream of the swirl element and close to the pick up tube

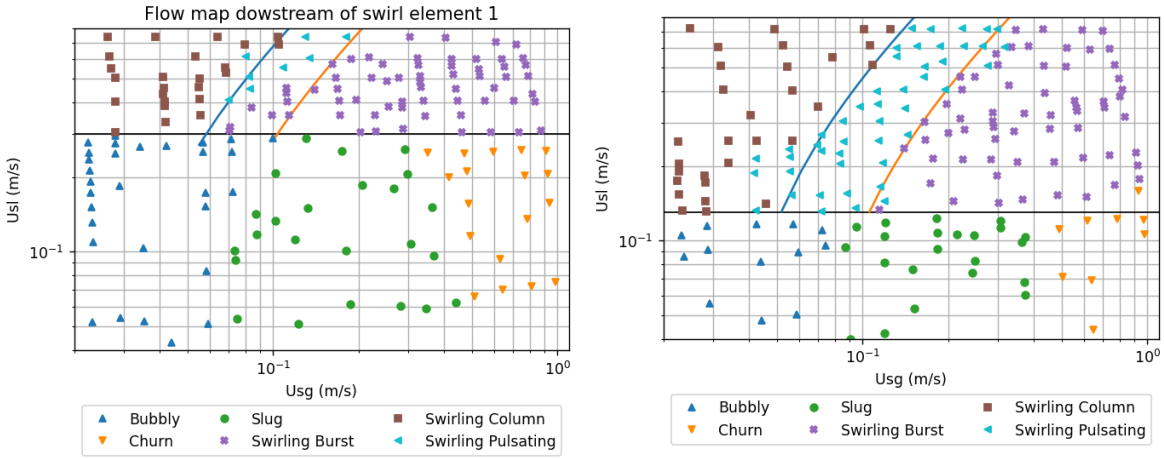

(a) (b)

Figure C.5: Flow pattern maps of swirl elements 1 and 3 with the transition lines between swirling column and swirling pulsating also shown

D

Importance of the individual terms of equations 3.16 and 3.20

In this appendix the importance of the individual terms of equations 3.16 and 3.20 are shown. This was done to visually show that for equation 3.16, u_θ depends much more on the gas flow rate for lower values of u_{sl} than for higher values of u_{sl}. Also shown are figures of the $\frac{R(R^2-R_g^2)}{R^3-R_g^3}$ and $\frac{1}{1-\alpha_g}$ terms to show their respective influences on u_θ.

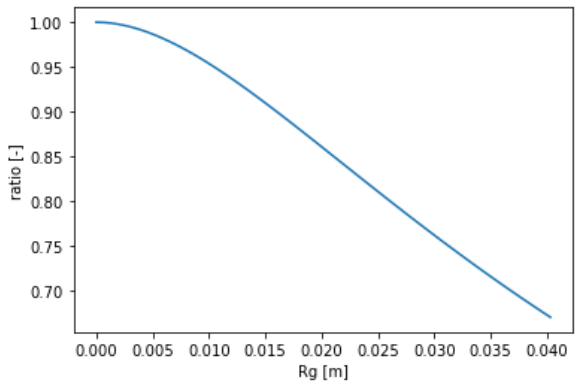

(a) Plot of the $\frac{R(R^2-R_g^2)}{R^3-R_g^3}$ term in equations 3.16 and 3.20

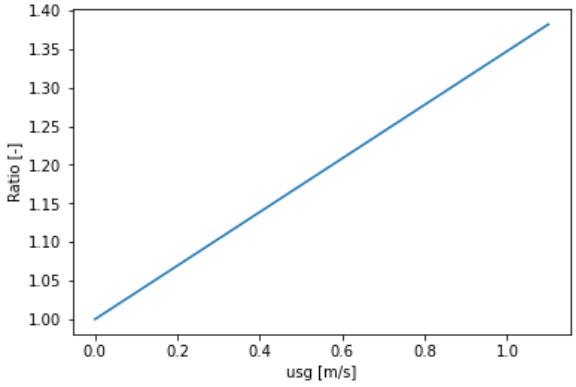

(b) Plot of the $\frac{1}{1-1.84\frac{u_{sg}}{u_{sg}}}$ term from equation 3.16 with an u_{sl} of 0.1 $\mathrm{m\,s^{-1}}$

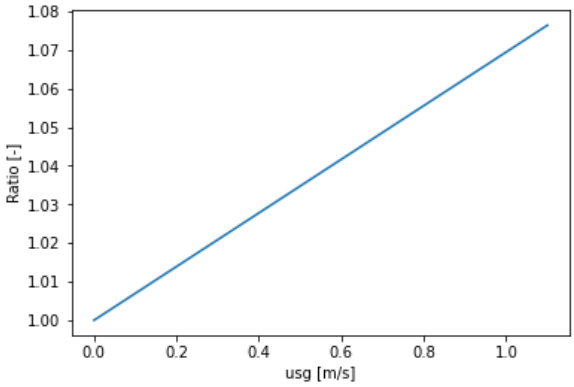

(c) Plot of the $\frac{1}{1-1.84\frac{u_{sg}}{u_{sg}}}$ term from equation 3.16 with an u_{sl} of 0.5 $\mathrm{m\,s^{-1}}$

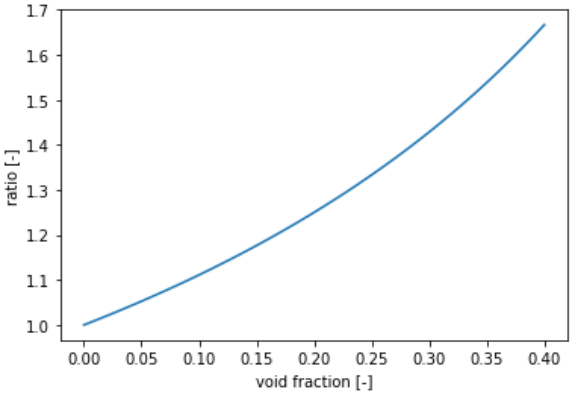

(d) Plot of the $\frac{1}{1-\alpha_g}$ term from equation 3.20

E

Detailed description for Shakutsui et. al.

The setup used in the papers of Shakutsui et al. [15, 16] make use of an tangential cyclone. Their pipe has an inner diameter of 30 mm. The cyclone itself has either 2 or 3 inlets with an diameter of 5 mm. It has a tapered section with a bottom diameter of 58 mm and a top diameter of 30 mm. An overview of their setup is shown in Figure E.1 With this information the speed at the entry of the tangential cyclone can be calculated by using the u_{sl} of the transition and ratio of cross-sectional pipe area and total inlet area

$$u_{inlet} = u_{sl} \frac{A_{pipe}}{n \cdot A_{inlet}} \tag{E.1}$$

Where u_{inlet} is the velocity at the tangential inlets, A_{pipe} is the cross-sectional area of the pipe, n is the number of inlets and A_{inlet} is the area of a single tangential inlet. The inlet velocity will also be the u_θ as the flow enters the cyclone via a tangential inlet. Doing this for both papers yields an u_θ of 3.6 m s^{-1}. This u_θ is corrected for the tapered cyclone according to

$$u_{\theta,pipe} = u_{\theta,inlet} \frac{R_{bottom}}{R_{pipe}} \tag{E.2}$$

Where R_{bottom} is the radius at the bottom of the cyclone and R_{pipe} is the pipe radius. For the bottom radius a value of 26.5 mm is used as this is the average position of the flow, assuming that this forms a layer of 5 mm thick. Doing this yields a $u_{\theta,pipe}$ of 6.96 m s^{-1}.

The flow patterns in their setup were recorded at 600 mm downstream of the tangential cyclone. Similar to the results shown in 5.2, u_θ has to be decayed in order to get a indication of the value at their observation point. This is done using equation 2.21 with an decay factor of 0.04 and a z of 600 mm. Doing this yields an u_θ of 2.85 m s^{-1} at the transition from non-columnar to columnar flow types.

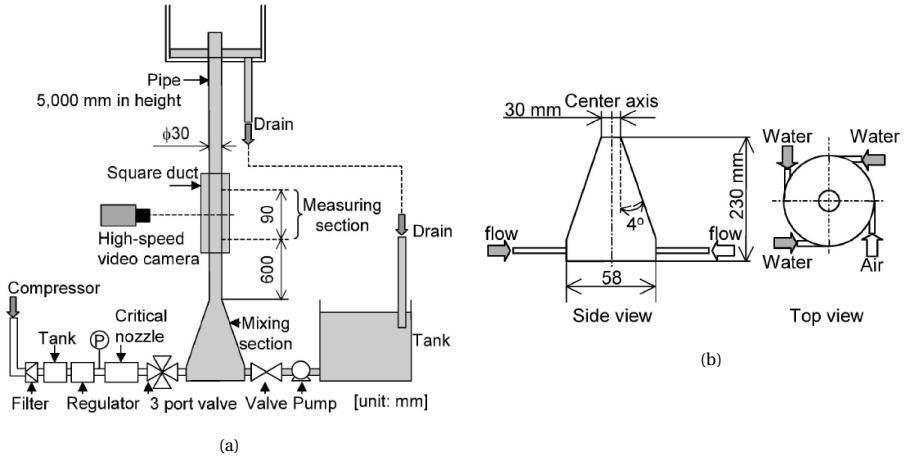

Figure E.1: An overview of the experimental setup used in Shakutsui et al.[16]